SANDIA REPORT

SAND2013-7989
Unlimited Release
Printed September, 2013

A Review of Macroscopic Ductile Failure Criteria

Edmundo Corona, Benjamin Reedlunn

Prepared by
Sandia National Laboratories
Albuquerque, New Mexico 87185 and Livermore, California 94550

Sandia National Laboratories is a multi-program laboratory managed and operated by Sandia Corporation, a wholly owned subsidiary of Lockheed Martin Corporation, for the U.S. Department of Energy's National Nuclear Security Administration under contract DE-AC04-94AL85000.

Approved for public release; further dissemination unlimited.

Sandia National Laboratories

Issued by Sandia National Laboratories, operated for the United States Department of Energy by Sandia Corporation.

NOTICE: This report was prepared as an account of work sponsored by an agency of the United States Government. Neither the United States Government, nor any agency thereof, nor any of their employees, nor any of their contractors, subcontractors, or their employees, make any warranty, express or implied, or assume any legal liability or responsibility for the accuracy, completeness, or usefulness of any information, apparatus, product, or process disclosed, or represent that its use would not infringe privately owned rights. Reference herein to any specific commercial product, process, or service by trade name, trademark, manufacturer, or otherwise, does not necessarily constitute or imply its endorsement, recommendation, or favoring by the United States Government, any agency thereof, or any of their contractors or subcontractors. The views and opinions expressed herein do not necessarily state or reflect those of the United States Government, any agency thereof, or any of their contractors.

Printed in the United States of America. This report has been reproduced directly from the best available copy.

Available to DOE and DOE contractors from
U.S. Department of Energy
Office of Scientific and Technical Information
P.O. Box 62
Oak Ridge, TN 37831

Telephone: (865) 576-8401
Facsimile: (865) 576-5728
E-Mail: reports@adonis.osti.gov
Online ordering: http://www.osti.gov/bridge

Available to the public from
U.S. Department of Commerce
National Technical Information Service
5285 Port Royal Rd
Springfield, VA 22161

Telephone: (800) 553-6847
Facsimile: (703) 605-6900
E-Mail: orders@ntis.fedworld.gov
Online ordering: http://www.ntis.gov/help/ordermethods.asp?loc=7-4-0#online

SAND2013-7989
Unlimited Release
Printed September, 2013

A Review of Macroscopic Ductile Failure Criteria

Edmundo Corona, Benjamin Reedlunn

Abstract

The objective of this work was to describe several of the ductile failure criteria commonly used to solve practical problems. The following failure models were considered: equivalent plastic strain, equivalent plastic strain in tension, maximum shear, Mohr-Coulomb, Wellman's tearing parameter, Johnson-Cook and BCJ_MEM. The document presents the main characteristics of each failure model as well as sample failure predictions for simple proportional loading stress histories in three dimensions and in plane stress. Plasticity calculations prior to failure were conducted with a simple, linear hardening, J_2 plasticity model. The resulting failure envelopes were plotted in principal stress space and plastic strain space, where the dependence on stress triaxiality and Lode angle are clearly visible. This information may help analysts select a ductile fracture model for a practical problem and help interpret analysis results.

Contents

Nomenclature . . . 8
1 Introduction . . . 11
1.1 Background . . . 11
1.2 Deformation/Failure Model Coupling . . . 15
1.3 Implementation in Finite Element Analysis . . . 16
1.4 Objectives . . . 18
2 Useful Concepts in Ductile Failure . . . 19
3 Failure Under Proportional Stress Paths . . . 24
3.1 Three-Dimensional Principal Stress Space . . . 24
3.2 Plane Stress . . . 27
4 Failure Criteria . . . 30
4.1 Equivalent Plastic Strain . . . 30
4.2 Equivalent Plastic Strain in Tension . . . 33
4.3 Maximum Shear Stress . . . 36
4.4 Mohr-Coulomb . . . 40
4.5 Tearing Parameter . . . 45
4.6 Johnson-Cook . . . 50
4.7 BCJ_MEM . . . 57
5 Summary . . . 64
References . . . 66

Figures

1 Strain to failure vs. triaxiality trend found by Bao and Wierzbicki (2004) for Al 2024-T351. . . . 14
2 Strain to failure vs. triaxiality trend found by Haltom *et al* (2013) for Al 6061-T6 from tension-torsion tests on tubular specimens. . . . 15
3 Sketch of an equivalent stress-plastic-strain curve showing the failure point and the subsequent stress decay over an additional strain ε_d^p. . . . 17
4 Principal stress space. . . . 21
5 The π plane. . . . 22
6 (a) Linear stress-plastic-strain curve with parameters and (b) schematic of failure contours in principal stress space. . . . 24
7 Definition of plane stress example parameters. (a) Stress-strain relationship parameters, (b) plane stress condition and (c) radial stress path. . . . 28
8 Plane stress space showing three regions where calculations will be conducted. 29
9 Stress and plastic strain states at failure according to the equivalent plastic strain failure criterion for 3D proportional stress paths. (a) Stress space and (b) plastic strain space. . . . 31

10 The equivalent plastic strain failure surface in principal stress space for 3D proportional stress paths. The hydrostatic axis is shown in green and the origin is shown by the intersection of the three red axes. The black line is the intersection with the σ_x-σ_y plane. 32
11 Equivalent plastic strain failure criterion for plane stress, proportional stress paths. (a) Stress space, (b) in-plane plastic strain space and (c) critical equivalent plastic strain vs. stress triaxiality. 33
12 The equivalent plastic strain in tension failure surface in principal stress space for 3D proportional stress paths. The hydrostatic axis is shown in green and the origin is shown by the intersection of the three red axes. The black line is the intersection with the σ_x-σ_y plane. 34
13 Equivalent plastic strain in tension failure criterion for plane stress, proportional stress paths. (a) Stress space, (b) in-plane plastic strain space, (c) critical equivalent plastic strain vs. stress triaxiality. 35
14 Stress and plastic strain states at failure according to the maximum shear stress failure criterion for 3D proportional stress paths. (a) Stress space and (b) plastic strain space. 37
15 The maximum shear criterion failure surface in principal stress space for 3D proportional stress paths. The hydrostatic axis is shown in green and the origin is shown by the intersection of the three red axes. The black line is the intersection with the σ_x-σ_y plane. 38
16 Maximum shear stress failure criterion for plane stress, proportional stress paths. (a) Stress space, (b) in-plane plastic strain space and (c) critical equivalent plastic strain vs. stress triaxiality. The results from the equivalent plastic strain criterion are shown for reference in blue line. 39
17 Stress and plastic strain states at failure according to the Mohr-Coulomb failure criterion for 3D proportional stress paths. (a) Stress space, $c_1 = 0.2$, (b) plastic strain space, $c_1 = 0.2$, (c) stress space, $c_1 = 0.4$ and (d) plastic strain space, $c_1 = 0.4$. 42
18 The Mohr-Coulomb failure surface in principal stress space for 3D proportional stress paths ($c_1 = 0.2$). The hydrostatic axis is shown in green and the origin is shown by the intersection of the three red axes. The black line is the intersection with the σ_x-σ_y plane. 43
19 Mohr-Coulomb failure criterion for plane stress, proportional stress paths. (a) Stress space, (b) in-plane plastic strain space, (c) critical equivalent plastic strain vs. stress triaxiality. The results from the equivalent plastic strain criterion are shown for reference in blue line. 45
20 Stress and plastic strain states at failure according to the tearing parameter failure criterion for 3D, proportional stress paths. (a) Stress space, $\xi = 4$, (b) plastic strain space, $\xi = 4$, (c) stress space, $\xi = 1$ and (d) plastic strain space, $\xi = 1$. 47
21 Predicted variation by the tearing parameter for the critical value of the equivalent plastic strain with triaxiality for three values of α and two values of ξ. . 48

22 The tearing parameter failure surface in principal stress space for 3D proportional stress paths ($\xi = 1$). The hydrostatic axis is shown in green and the origin is shown by the intersection of the three red axes. The black line is the intersection with the σ_x-σ_y plane. 49
23 Tearing parameter failure criterion for plane stress, proportional stress paths. (a) Stress space, (b) in-plane plastic strain space, (c) critical equivalent plastic strain vs. stress triaxiality. The results from the equivalent plastic strain criterion are shown for reference in blue line. 51
24 Stress and plastic strain states at failure according to the Johnson-Cook failure criterion for 3D proportional stress paths. (a) Stress space, case 1, (b) plastic strain space, case 1, (c) stress space, case 2 and (d) plastic strain space, case 2. Case 1: $d_1 = 0.005, d_2 = 0.34, d_3 = -1.5$. Case 2: $d_1 = 0.005, d_2 = 0.39415, d_3 = -3$. 54
25 The Johnson-Cook failure surface in principal stress space for 3D proportional stress paths ($d_1 = 0.005, d_2 = 0.34, d_3 = -1.5$). The hydrostatic axis is shown in green and the origin is shown by the intersection of the three red axes. The black line is the intersection with the σ_x-σ_y plane. 55
26 The Johnson-Cook failure criterion for plane stress, proportional stress paths. The two cases shown correspond to those shown in Fig. 24. (a) Stress space, (b) in-plane plastic strain space, (c) critical equivalent plastic strain vs. stress triaxiality. The results from the equivalent plastic strain criterion are shown for reference in blue line. 56
27 The BCJ_MEM failure surface ($m = 7.0$) in principal stress space for 3D proportional stress paths. The plane stress curve depicts the intersection of the failure surface with the σ_x-σ_y plane. 60
28 The BCJ_MEM failure surface ($m = 7.0$) for 3D, proportional, stress paths, projected onto the π-plane. The contours in (a) and (b) show that the failure model does not depend on the Lode angle. 61
29 The BCJ_MEM failure surface perpendicular to the hydrostatic axis for several values of m. 62
30 The BCJ_MEM failure criterion ($m = 7.0$) for plane stress, proportional stress paths. The results of the equivalent plastic strain criterion are shown for reference in blue line. 63

Tables

1 General Variables 8
2 Model Specific Variables 9
3 Summary of ductile failure criteria considered. 64

Nomenclature

Table 1: General Variables

Symbol	Definition
E	Young's modulus
E_t^p	Plastic tangent modulus
f	Yield function
I_1, I_2, I_3	Stress invariants
J_1, J_2, J_3	Deviatoric stress invariants
s_{ij}	Deviatoric stress components
s_x, s_y, s_z	Principal deviatoric stress components
s	Prescribed value of s_x
s_c	Calculated value of s at failure
T	Absolute temperature
α	Deviatoric stress proportionality factor
β	Stress proportionality factor in plane stress
ε_x^p, ε_x^p, ε_x^p	Principal plastic strain components
ε_e^p	Equivalent plastic strain
ε_{et}^p	Equivalent plastic strain in tension
ε_f^p	Uniaxial plastic strain at failure
η	Stress triaxiality (σ_m/σ_e)
θ	Lode angle
μ	Shear modulus
ν	Poisson's ratio
σ_{ij}	Stress tensor components
σ_x, σ_y, σ_z	Principal stress components
σ_1, σ_2, σ_3	Principal stress components, ordered as $\sigma_1 \geq \sigma_2 \geq \sigma_3$
σ	Prescribed value of σ_x in plane stress
σ_c	Calculated value of σ at failure
σ_e	Equivalent stress
σ_{ec}	Calculated value of σ_e at failure
σ_f	Uniaxial stress at failure
σ_m	Mean or hydrostatic stress
σ_o	Initial uniaxial yield strength
σ_y	Current uniaxial yield strength
σ_o	Value of σ at initial yield
$\tau_{\max}$	Maximum shear stress
ϕ	Triaxiality angle

Table 2: Model Specific Variables

Symbol	Definition
A, B, n, C, m	Parameters of the Johnson-Cook strength model
c_1, c_2	Mohr-Coulomb failure criterion constants
d_1, d_2, d_3, d_4, d_5	Parameters of the Johnson-Cook failure criterion
T_r, T_m, $\hat{T}$	Reference, melting, and homologous temperature
ψ	Tearing parameter
ψ_f	Critical tearing parameter value at failure
ξ	Tearing parameter exponent
v	BCJ_MEM damage parameter
v_o	BCJ_MEM damage parameter value at initialization
v_f	BCJ_MEM damage parameter value at failure
m	BCJ_MEM damage exponent
R_d	BCJ_MEM dynamic recovery parameter
w	BCJ_MEM equivalent plastic strain flow rate parameter
r	BCJ_MEM equivalent plastic strain flow rate exponent
τ_f	Failure value of $\tau_{\max}$ in maximum shear criterion

1 Introduction

Many practical problems of interest at Sandia are concerned with the response of engineering structures[1] to high intensity loads that may take them well beyond their design limits. In the case of metallic structures, this raises the possibility of tearing after large deformations have exhausted the ductility of the material. This type of failure is commonly called ductile failure or ductile tearing.

Ductile failure in metals is a topic that has received significant attention in the literature for over 50 years. Tearing is the macroscopic result of deformation and failure phenomena that occur at the micro-structural level of the material. Calculations at the micro-structural level still seem beyond the realm of possibility for engineering-level applications. Currently, most calculations make use of phenomenological failure models instead. This type of model describes phenomena observed at the macro scale without explicitly considering microscopic factors such as the physics of atomic lattices, etc. A good example is classical plasticity, which is constructed to represent observed plastic deformation of metals without explicitly modeling dislocation motion in atomic lattices that are in turn embedded in polycrystalline media.

It must be noted as well that macroscopic effects such as the presence of stress concentrators and the development of local instabilities are important in the prediction of failure because they can locally induce large strains that exhaust the ductility of the material. Since the strain in the material depends on the loading history and the material behavior, the prediction of failure depends not only on the conditions at failure, but also on the adequate calculation of the stress and material deformation histories prior to failure.

1.1 Background

The field of ductile failure of metals is vast and can be very complex. See, for example, the survey article by Garrison and Moody (1987), which discusses various aspects of this topic. Factors that can influence material failure include, for example, the current states of stress and strain, the loading history, the strain rate, the temperature and the properties of the material. Each of these items can be sub-divided into more specific quantities. For example, the effect of the state of stress can be attributed to the value of the hydrostatic mean stress and the invariants of the deviatoric stress. In the case of material properties, the yield stress, the dependence of the plastic tangent modulus on equivalent strain, the dependence of the strain-to-failure on the stress invariants, and the initial yield anisotropy plus its evolution with deformation can affect the results of failure calculations. Parameters related to the thermo-mechanical and strain-rate dependencies of the constitutive and failure models are also in this category.

The work presented in this report was conducted over a period of a few months, and

[1] The term *structures* is used here to denote general objects made of solid materials.

therefore can only begin to scratch the surface of this important field. Its focus will be on current thinking from the mechanics of solids perspective and on some of the common failure models used in the finite element analysis of structures. Analysts must be aware that a significant gap exists between the leading edge of research and the use of failure models in practical applications. Also, experts in the field believe that significantly more research is necessary before ductile failure can be reliably predicted in everyday engineering analysis. As is often the case, however, applied engineering and design require the use of models that, although they may not be entirely accurate, provide at least some realistic estimate of the load levels that are likely to induce failure in a structure. This insight can then be used to suggest appropriate testing and to recommend design margins.

One of the seminal observations regarding the ductility of metals was published by Bridgman (1945), who carried out experimental studies where uniaxial tension tests were conducted on steel specimens while under hydrostatic pressure. The most striking effect that he observed was a great increase in ductility with increasing pressure. In other words, the specimens could support significantly larger strains and much more severe necking prior to failure when pulled in the presence of pressure. The implication of Bridgman's observation is that the ductility of metals is strongly dependent on the hydrostatic component of the stress tensor. The higher the hydrostatic stress (defined as positive when tensile) the lower the strain at failure.

Bridgman also observed that, to a first approximation, the flow stress for a given value of strain was independent of pressure. In fact, classical plasticity theory assumes that plastic deformation depends only on the deviatoric stress components and is incompressible.

Early theoretical treatment of the effect of the hydrostatic stress on the observed ductility of metals was conducted by McClintock (1968) and by Rice and Tracey (1969). Their work was motivated by evidence of growth and coalescence of voids observed in experiments. Both works used micro-mechanics to look at void growth during plastic deformation and showed that the void growth rate in an elastic-plastic material depends strongly on the value of the far-field hydrostatic stress. The larger the hydrostatic stress, the faster the voids can grow. Since they attributed ductile failure to the coalescence of voids, a higher mean hydrostatic stress correlates with decreased ductility.

Currently, it is generally accepted that the mechanisms behind ductile failure occur at the grain scale. These mechanisms are heavily influenced by inclusions introduced by alloying, as described in the introduction of the paper by Ghahremaninezhad and Ravi-Chandar (2012). The differences in stiffness between the inclusions and the bulk material, as well as the fracture of the inclusions, can provide the "seeds" for the nucleation of voids under favorable macroscopic states of stress. Once nucleated, the voids can grow and coalesce to produce macroscopic cracks and induce ductile tearing of the material.

One current topic of research concerns the stage at which the voids nucleate and how fast they grow. Recent experimental work presented in Ghahremaninezhad and Ravi-Chandar (2011) and Ghahremaninezhad and Ravi-Chandar (2012) for polycrystalline OFHC copper and Al 6061-T6 respectively showed that, at least for these two materials, the growth of voids

remained subdued even after very large strains had accumulated. Furthermore, post-failure SEM imaging revealed very little void growth just a short distance (30 μm) away from the fracture plane for Al 6061-T6. These observations suggest ductile failure is caused by sudden, highly localized, void nucleation and growth that occur after significant plastic deformation. This is in contrast to images of sectioned specimens shown by Puttick (1959) where significant voiding is visible over relatively large regions. Ghahremaninezhad and Ravi-Chandar (2011), however, caution that the characteristics of void nucleation and growth can depend on the specific material considered.

Another area that warrants attention is ductile failure under shear-dominated states of stress, where the mean hydrostatic stress is near zero. Observations have shown evidence of growth and coalescence of voids in these cases (see, for example, SEM fractographs in Ghahremaninezhad and Ravi-Chandar (2013)). Thus, the dependence of failure on the hydrostatic stress can be more complex than has been suggested by the work of Rice and Tracey (1969). In fact, failure models that tie void growth to a positive hydrostatic mean stress must be modified to predict shear dominated failure (see Nashon and Hutchinson (2008), for an example).

Another issue that has received significant attention in the last 10 years is a curious trend that was found by Bao and Wierzbicki (2004). They performed tests on 2024-T351 aluminum alloy specimens of various shapes all cut from the same block of material. The specimens included smooth and notched tension specimens, flat shear specimens and compression round upsetting specimens. Bao and Wierzbicki then matched a finite element model of each test to the measured engineering stress strain curve, and used the model to determine the equivalent plastic strain to failure. When plotting the equivalent plastic strain to failure against triaxiality across all the tests, they found the trend shown in Fig. 1. Clearly, the resulting curve does not monotonically decrease with triaxiality, as suggested previously. Rather, it exhibits a cusp at a triaxiality of 0.4 and a range between 0 and 0.4 where the strain to failure *increases* with triaxiality. The presence of the cusp has also been reported by Barsoum and Faleskog (2007) for Weldox 420 and Weldox 960 steel notched tubular specimens under tension and torsion. The values of triaxiality where the cusps occurred, however, varied between 0.8 and 1.0, and experiments were not shown for triaxialities below 0.3.

Recent work by Ghahremaninezhad and Ravi-Chandar (2013) on 6061-T6 aluminum alloy under shear-dominated loading induced in an Arcan-like specimen, however, indicated a simpler trend where the strain to failure monotonically decreases with triaxiality. These observations were further reinforced for the same material by Haltom *et al* (2013), who conducted a series of tension-torsion experiments on thin-walled tubular specimens. Their results are shown in Fig. 2.

Whether the differences between the two sets of data are due to the different materials used in the studies or to other causes is an outstanding issue in the field. In a recent publication, Beese *et al* (2010) found a trend similar to that in Fig. 1 for Al 6061-T6 sheets using a series of tests on specimens with different geometries. This is nominally the same alloy investigated by Haltom *et al* (2013). The products from which the specimens were

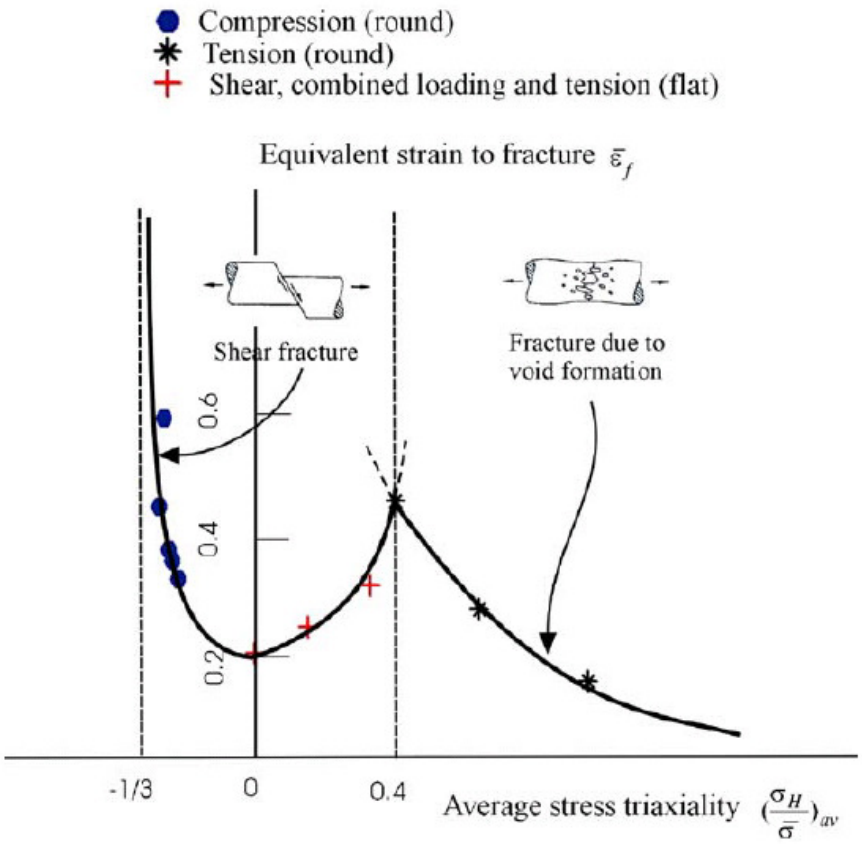

Figure 1: Strain to failure vs. triaxiality trend found by Bao and Wierzbicki (2004) for Al 2024-T351.

machined, however, were different; sheet vs. tube. The trend shown in Fig. 1, prompted Weirzbicki and several of his students at MIT to propose that the strain to failure must depend not only on triaxiality, but also on the Lode angle[2] and to develop models where the strain to failure depends on these two factors. See, for example, Bai and Wierzbicki (2008). The idea of including Lode angle dependence in failure models has gained some traction and was implemented in the 6.12 version of Abaqus. The calibration of such models, however, requires significant work that is not straight-forward and for which more guidance needs to be developed.

The issue of calibration brings another aspect of great importance when using ductile failure models that has been demonstrated by the work presented in Ghahremaninezhad and Ravi-Chandar (2011), Ghahremaninezhad and Ravi-Chandar (2012), Ghahremaninezhad and Ravi-Chandar (2013) and Haltom *et al* (2013). These works show that the strains to failure measured in tests are highly sensitive to the 'gage length' used to make strain measurements. The reason for this is that failure tends to occur in regions undergoing strain localization within relatively narrow bands. Therefore, strains measured inside the localiza-

[2]See Section 2 for definitions of terms used in this report.

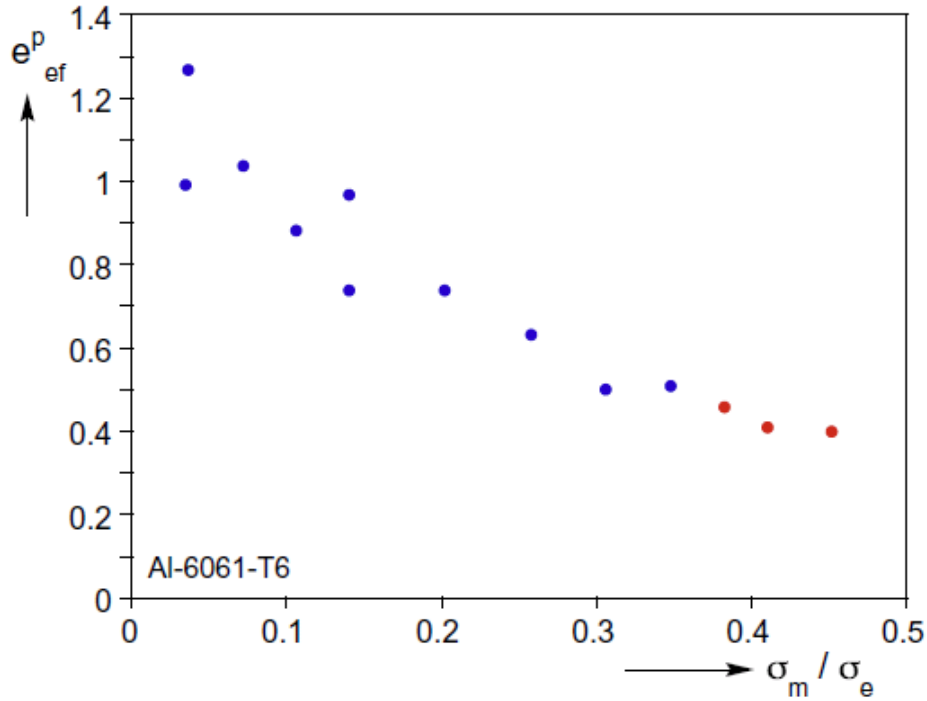

Figure 2: Strain to failure vs. triaxiality trend found by Haltom *et al* (2013) for Al 6061-T6 from tension-torsion tests on tubular specimens.

tion regions using the grain size as the gage length will be much higher than strains measured over a larger gage length that includes the localization zone and some material outside of it that is less strained. This issue is not only important for experimentalists reporting their measurements but also for analysts who need to calibrate their finite element models because it demonstrates the role that element size can play in failure calculations. Ideally, finite element models used in the calibration of ductile failure models and in the solution of problems should have element sizes that can resolve the localization and failure phenomena observed in both the calibration tests and the applications of interest. This allows the strain to be calculated locally in the failure region. If it is impossible to utilize small enough elements to meet this recommendation, then allowances need to be made for the larger element size, most likely involving smaller strains to failure. Keep in mind, however, that making this kind of allowances may diminish the ability to capture ductile failure accurately.

1.2 Deformation/Failure Model Coupling

Although it may be possible to construct micromechanics models that explicitly model voids or other damage mechanisms, alternative approaches must be considered when addressing practical engineering problems at the macroscopic scale to keep the analysis tractable. It appears that two categories of models are currently available to model plastic deformation and ductile failure: coupled and uncoupled.

Coupled Models: In these models the calculation of the plastic deformations is coupled with calculations of material damage, which can be taken to represent the growth of voids in the material. As a result, the development of damage influences the inelastic response and vice-versa. In these models, the material response may soften after sufficient damage has accumulated, and failure can be taken to occur when the material damage reaches a critical value. Examples include models based on the work of Gurson (1977) such as the model presented by Tvergaard (1981) and the BCJ-MEM model (Sierra Solid Mechanics Team, 2013) developed at SNL-CA. As discussed earlier, these models in general predict little void growth when the state of stress is shear dominated, thus delaying or preventing the onset of failure in this regime. Modifications like the one developed by Nashon and Hutchinson (2008) have been proposed to remedy this issue.

Uncoupled Models: In these models the calculation of plastic deformation is conducted assuming no damage in the material. A failure criterion is evaluated during plastic deformation based on the stress and strain histories. Material failure is taken to occur when the failure criterion reaches a critical value. In these models the material response typically hardens, or is perfectly plastic, until failure. In most engineering structural analyses, the J_2 flow theory of plasticity is used to calculate the plastic deformation. Examples of these models include the Johnson-Cook model (Johnson and Cook, 1985) and the MLEP-Failure model developed by Wellman (2012).

The present work will concentrate on models likely to be considered by analysts at SNL. These include several uncoupled failure models that can be used in conjunction with J_2 plasticity as well as the BCJ-MEM coupled model.

1.3 Implementation in Finite Element Analysis

Finite element analysis of solids and structures has become commonplace in engineering work. Naturally, some analyses relate to the calculation of loads that may cause ductile failure in structures. Therefore is it highly desirable to implement available failure criteria in finite element codes to enable the failure predictions.

The calculation of material failure in finite element analysis can be considered to consist of three stages as follows:

1. From the time that plastic yielding is first detected, a state variable is calculated that represents the amount of damage that has been induced in the material. This variable is calculated at each integration point in the model. The state variable may represent void nucleation and growth in coupled models, or simply a quantity related to the state of stress or plastic strain accumulation in uncoupled models. At each step of the calculations, the value of this state variable is compared to a critical value. As long as the current value of the state variable is below critical, the material has not failed. Material failure is declared when it reaches a critical value.

2. Once it has determined that material failure has occurred at an integration point, a decision must be made regarding whether to declare failure at the element level. If the element has a single integration point, then this decision is straight-forward and failure can be declared at the element level. For elements with multiple integration points, the number of integration points that must fail before element failure is declared must be prescribed in advance.

3. After failure is declared at the element level then the mesh must be modified to reflect the initiation or propagation of a crack. Several methods have been proposed to modify the mesh such as cohesive zone insertion, the extended finite element method (x-FEM) and element death. The latter is the easiest to implement and seemingly the one most frequently used one at SNL and elsewhere. In this method, the stress in the element must first be reduced to zero. This is followed by the removal of the element from the mesh to simulate the presence of a crack. If necessary, the element may be converted to a particle to conserve mass and to represent fragments. If not, the element and its mass are simply removed. The stress reduction can happen instantaneously or, as is often recommended, over additional straining as illustrated in Fig. 3. If the stress decays with further straining, more energy must be dissipated before the element is deleted. It is often recommended that the energy dissipated during the stress decay be adjusted to minimize the dependence of the failure calculations on the mesh as discussed by Wellman (2012).

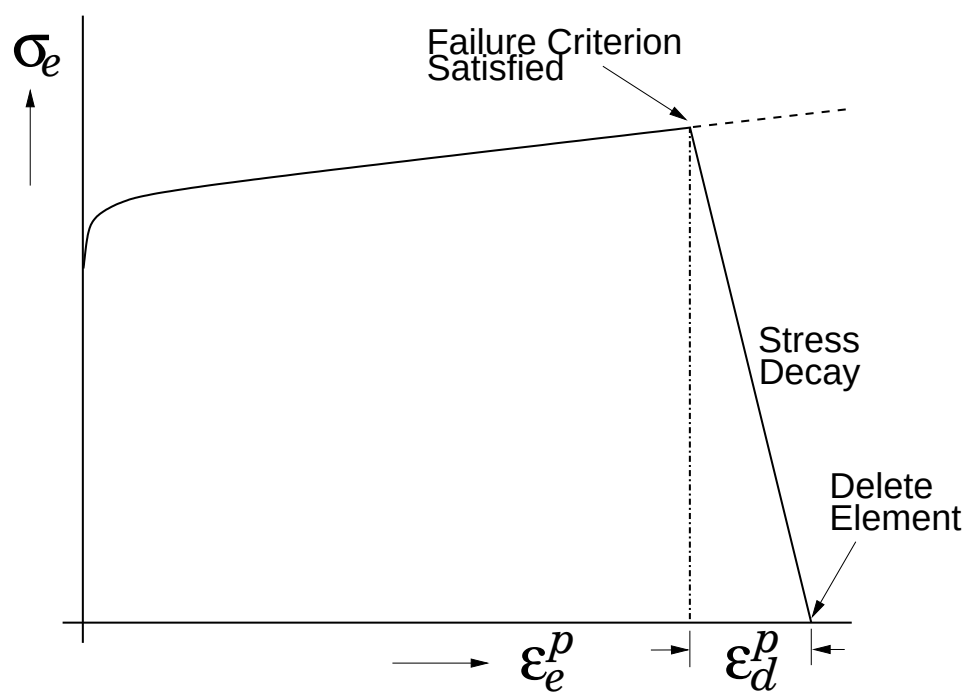

Figure 3: Sketch of an equivalent stress-plastic-strain curve showing the failure point and the subsequent stress decay over an additional strain ε_d^p.

1.4 Objectives

The original objective of the present work was to conduct a survey of ductile failure models available in the literature, and how they could be applied in problems involving thin-walled structures. Given the relative inexperience of the authors on the topic, however, the work soon became more of a learning experience. In order to better understand the models, the scope was extended to consider failure under three-dimensional states of stress. This change required that the number of models reviewed be reduced. In the end, this report is still written as a survey that considers a few commonly used failure criteria from a three-dimensional perspective. Simple, proportional load histories are used in the examples. This is followed by presentations of how the failure criteria project onto a plane stress state, which is characteristic of thin-walled structures. The report represents the current level of understanding by the authors, and the hope is that it will be a useful ductile failure reference for analysts working in the field.

2 Useful Concepts in Ductile Failure

The purpose of this section is to briefly list useful concepts that are needed to better follow the material to be presented in the next few sections. The intent is for readers to review the concepts that will be used in the discussions and results that follow. For the most part, no derivations from basic principles will be presented.

In-depth treatises of the topics of interest here can be found in many books in plasticity or continuum mechanics. In order to present concepts in as simple form as possible, an orthonormal basis is assumed and index notation will be used. For details on notation as well as continuum mechanics and plasticity concepts see, for example, Fung (1965) and Mendelson (1983).

Stress and traction: The components of the stress tensor are $\sigma_{ij} = \sigma_{ji}$ giving six independent components. The traction components on a surface with unit normal $\mathbf{n}$ are $T_i = \sigma_{ij} n_j$.

Principal stresses: The principal stress components $\sigma_x, \sigma_y, \sigma_z$ are the roots of the characteristic cubic equation

$$-\sigma^3 + I_1\sigma^2 + I_2\sigma + I_3 = 0 \tag{1}$$

where I_1, I_2 and I_3 are the stress invariants given by

$$\begin{aligned} I_1 &= \sigma_{ii} \\ I_2 &= -\frac{1}{2}\left(\sigma_{ii}\sigma_{jj} - \sigma_{ij}\sigma_{ji}\right) \\ I_3 &= \frac{1}{6}\varepsilon_{ijk}\varepsilon_{pqr}\sigma_{pi}\sigma_{qj}\sigma_{rk}, \end{aligned}$$

where ε_{ijk} is the Levi-Cevita tensor (also known as the alternating symbol).

Normal and shear traction components: The traction vector on a surface can be decomposed into normal and shear components. Given a surface with unit normal components n_i with respect to the prinicipal stress frame, the normal component is

$$\sigma_n = \sigma_1 n_1^2 + \sigma_2 n_2^2 + \sigma_3 n_3^2, \tag{2}$$

while the shear component is

$$\tau = \sqrt{n_1^2 n_2^2(\sigma_1 - \sigma_2)^2 + n_2^2 n_3^2(\sigma_2 - \sigma_3)^2 + n_3^2 n_1^2(\sigma_3 - \sigma_1)^2}. \tag{3}$$

Maximum shear stress: If the principal stresses are ordered such that $\sigma_1 \geq \sigma_2 \geq \sigma_3$ then the maximum shear stress is

$$\tau_{\max} = \frac{\sigma_1 - \sigma_3}{2}. \tag{4}$$

Mean hydrostatic stress: The mean hydrostatic stress (also called mean stress or hydrostatic stress) is given by

$$\sigma_m = \frac{1}{3}\sigma_{ii} = \frac{1}{3}I_1. \tag{5}$$

Deviatoric stress: The plastic deformation of metals is generally taken to be unaffected by the mean hydrostatic stress, so it is useful to decompose σ_{ij} into hydrostatic and deviatoric components as follows:

$$\sigma_{ij} = s_{ij} + \sigma_m \delta_{ij} \tag{6}$$

where s_{ij} are the components of the deviatoric stress and δ_{ij} is the Kronecker delta.

Invariants of the deviatoric stress: The three invariants of the deviatoric stress are:

$$J_1 = 0$$
$$J_2 = \frac{1}{2}s_{ij}s_{ij}$$
$$J_3 = \frac{1}{6}\varepsilon_{ijk}\varepsilon_{pqr}s_{pi}s_{qj}s_{rk}.$$

Equivalent von-Mises stress: The equivalent von-Mises stress is given by

$$\sigma_e = \sqrt{3J_2} = \sqrt{\frac{3}{2}s_{ij}s_{ij}}. \tag{7}$$

Stress triaxiality: The stress triaxiality is defined by

$$\eta = \frac{\sigma_m}{\sigma_e}. \tag{8}$$

Principal stress space: For ease of visualization, it is often convenient to refer to principal stress space, a three-dimensional space where the three principal stresses are plotted in orthogonal coordinates as shown in Fig. 4. Here, the state of stress represented by the vector **OP** can be decomposed into a component along the hydrostatic axis **QP** — along the direction (1,1,1) — and a component orthogonal to it, **OQ**. The magnitudes of these vectors are

$$|\mathbf{QP}| = \sqrt{3}\sigma_m$$
$$|\mathbf{OQ}| = \sqrt{2J_2} = \sqrt{\frac{2}{3}}\sigma_e.$$

The π-plane and Lode angle: The π-plane is defined in principal stress space as having unit normal along the hydrostatic axis $(\frac{1}{\sqrt{3}}, \frac{1}{\sqrt{3}}, \frac{1}{\sqrt{3}})$. The vector **OQ** in Fig. 4 lies on the π-plane as shown in Fig. 5. The polar angle θ shown is known as the *Lode angle*. It is given by

$$\sqrt{3}\tan\theta = (2\sigma_z - \sigma_y - \sigma_x)/(\sigma_y - \sigma_x) \tag{9}$$

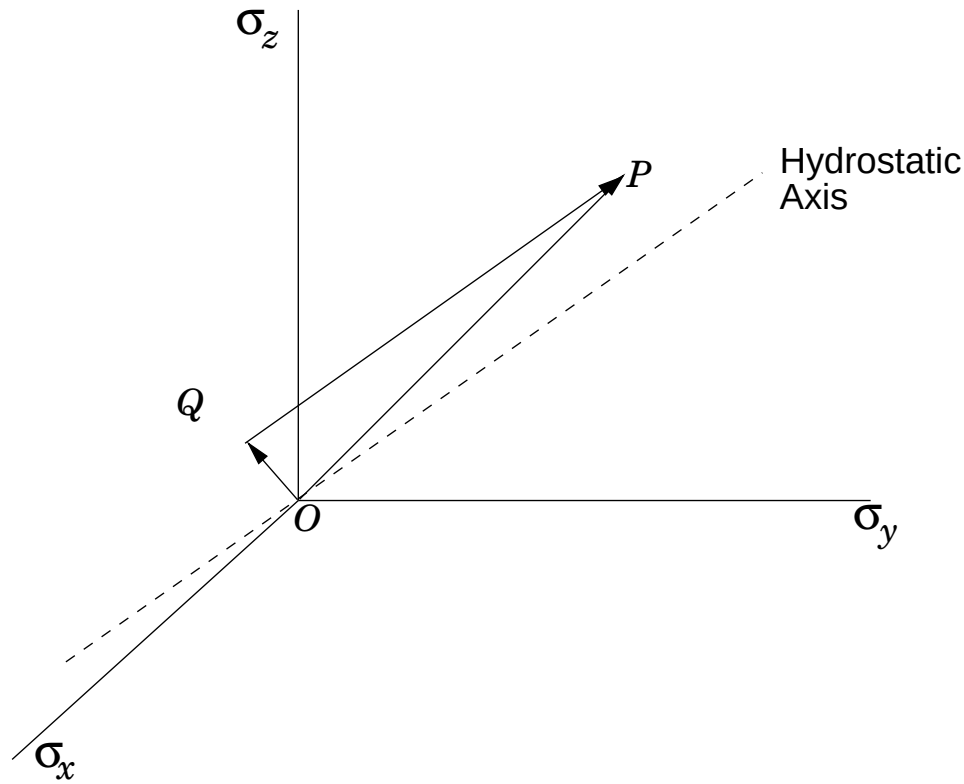

Figure 4: Principal stress space.

and has the range $-\frac{\pi}{6} \leq \theta \leq \frac{\pi}{6}$ in the example shown where $\sigma_y > \sigma_z > \sigma_x$. Note that the π-plane has six segments where the ordering of the principal stresses is different. The range of the Lode angle is the same, but the order of the stress components in (9) changes. For isotropic failure models the contours of the failure surface on planes parallel to the π-plane have the same shape in each of the segments. For these models it is sufficient to calculate their shape over one segment. The shapes in the other segments can be obtained by reflections about the stress axes.

Plasticity: Plasticity concerns the development of permanent deformations of the material. It depends on not only the current state of stress, but also the history of loading. As a result, flow theories of plasticity are formulated in an incremental fashion. Classical flow theories of plasticity have three principal components: a yield criterion, a flow rule and a hardening rule.

Yield criterion: A yield criterion is a hypersurface in stress space that encloses the states of stress where the material behavior is elastic (called the elastic region). Many yield criteria have been proposed for metals. In general, yielding in metals is taken to be insensitive to the mean hydrostatic stress. As a result, the surfaces representing the yield criteria are cylinders aligned parallel to the hydrostatic axis when plotted in principal stress space. The most common yield criterion used for metals is the von-Mises criterion. It can be written as $f = \sigma_e - \sigma_o$, where σ_o is the yield stress. Plastic deformation becomes possible when the current

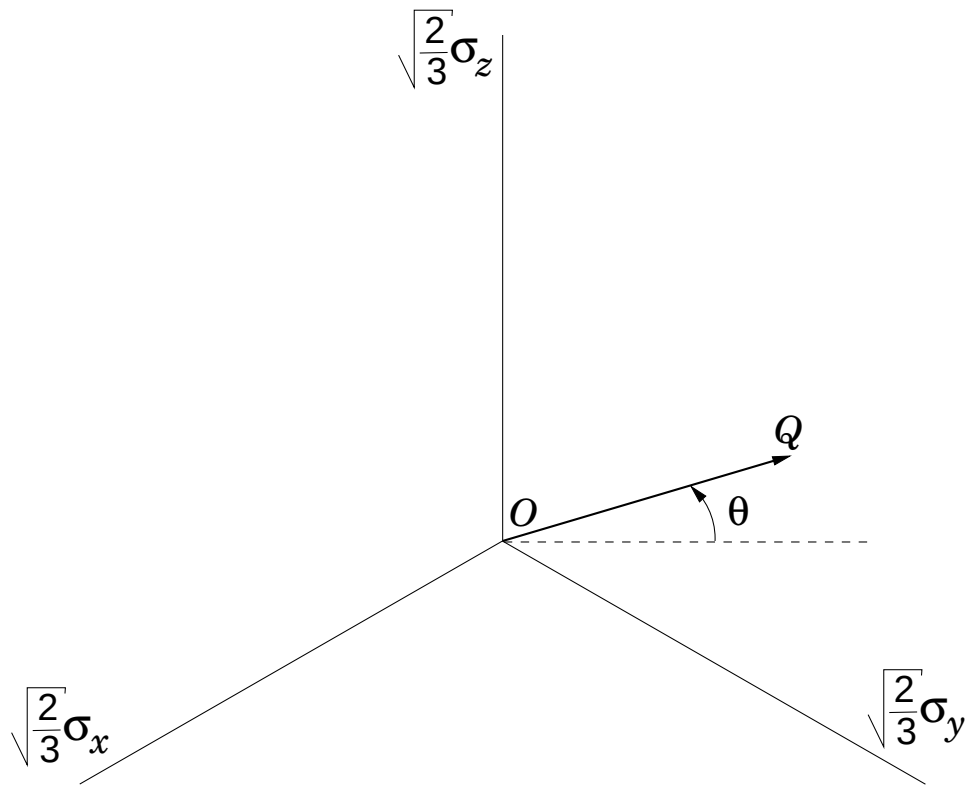

Figure 5: The π plane.

stress is on the yield surface, that is when $f = 0$. Under these conditions, if an increment in stress points away from the elastic region, then plastic deformation occurs. Otherwise the material response is elastic. For plasticity calculations, the initial yield stress is taken as the proportional limit. In principal stress space the von-Mises criterion is a cylinder of circular cross-section.

Flow rule: The flow rule is the relationship between the stress increment ($\mathrm{d}\sigma_{ij}$) and the plastic strain increment ($\mathrm{d}\varepsilon^p_{ij}$) during plastic flow. It is given by

$$\mathrm{d}\varepsilon^p_{ij} = G\frac{\partial f}{\partial \sigma_{ij}}\frac{\partial f}{\partial \sigma_{mn}}\mathrm{d}\sigma_{mn}$$

where $G = G(\sigma_{ij}, \varepsilon_{ij}, \text{history})$. The total strain increment is given by

$$\mathrm{d}\varepsilon_{ij} = \mathrm{d}\varepsilon^e_{ij} + \mathrm{d}\varepsilon^p_{ij}$$

where $d\varepsilon^e_{ij}$ is the linearly elastic strain increment given by

$$\mathrm{d}\varepsilon^e_{ij} = \frac{1+\nu}{E}\mathrm{d}\sigma_{ij} - \frac{\nu}{E}\mathrm{d}\sigma_{kk}\delta_{ij}$$

and E, ν are the Young's modulus and Poisson's ratio of the material.

Hardening Rule: During plastic deformation, the current stress has to remain on the yield surface so that the elastic region is immediately available upon unloading.

This requirement is called the *consistency condition*. Therefore, the yield surface changes during plastic deformation. The hardening rule prescribes how the yield surface changes. The most common hardening rule is isotropic hardening, where the yield surface retains its shape and simply grows in size. In this case, the current yield stress of the material is taken to be equal to the maximum equivalent stress achieved up to the present, $\sigma_o = \sigma_e^{\max}$ Other possibilities include kinematic hardening, where the yield surface translates without changing shape and combined isotropic/kinematic hardening. Hardening rules that allow the yield surface to change shape are also possible, but exhibit considerable complexity.

J_2 **flow theory with isotropic hardening:** Here, the yield function is that of von-Mises so the equivalent stress is given by (7). An equivalent plastic strain increment, $d\varepsilon_e^p$, is defined so that

$$\sigma_e \mathrm{d}\varepsilon_e^p = \sigma_{ij} \mathrm{d}\varepsilon_{ij}^p \tag{10}$$

and is given by

$$\mathrm{d}\varepsilon_e^p = \sqrt{\frac{2}{3} \mathrm{d}\varepsilon_{ij}^p \mathrm{d}\varepsilon_{ij}^p}. \tag{11}$$

The flow rule reduces to

$$\mathrm{d}\varepsilon_{ij}^p = \frac{9}{4\sigma_e^2} \frac{1}{E_t^p} s_{ij} s_{mn} \mathrm{d}\sigma_{mn} \tag{12}$$

where E_t^p is the current value of the plastic tangent modulus. As mentioned above, during plastic deformation the hardening rule changes the yield surface to $f = \sigma_e - \sigma_e^{\max} = 0$.

3 Failure Under Proportional Stress Paths

The prediction of ductile failure is fairly complex and is dependent on the plastic deformation of the material. As a result, failure can be sensitive to the loading path, or stress history, as has been discussed by Stoughton and Yoon (2012). The failure criteria that will be considered in Section 4 exhibit some form of path dependence, but there is no expectation that they will reflect the path dependence describted by Sotoughton and Yoon. In order to give the reader an idea of how predictions obtained with various failure models compare, simple proportional loading examples were constructed in both three-dimensional principal stress space as well as plane stress space as described in the next two sections.

3.1 Three-Dimensional Principal Stress Space

Suppose that we have an elastic-plastic material with the uniaxial stress-plastic strain curve shown in Fig. 6(a). It has yield stress σ_o and constant plastic tangent modulus E_t^p. Under uniaxial stress, failure is taken to occur when the plastic strain is equal to ε_f^p. The corresponding stress value is σ_f. Let the material be loaded incrementally in principal stress space starting from the unloaded state while keeping a constant proportion between the stress components. Such proportional loading gives stress paths such as **OA** or **OB** in Fig. 6(b) that are straight lines. The direction of the stress path can be defined by two angles, ϕ and θ as shown in the figure. ϕ is the angle that the stress path makes with respect to the hydrostatic axis and is directly related to the stress triaxiality η by

$$\tan\phi = \frac{\sqrt{2}}{3}\left(\frac{\sigma_e}{\sigma_m}\right) = \frac{\sqrt{2}}{3}\frac{1}{\eta}. \tag{13}$$

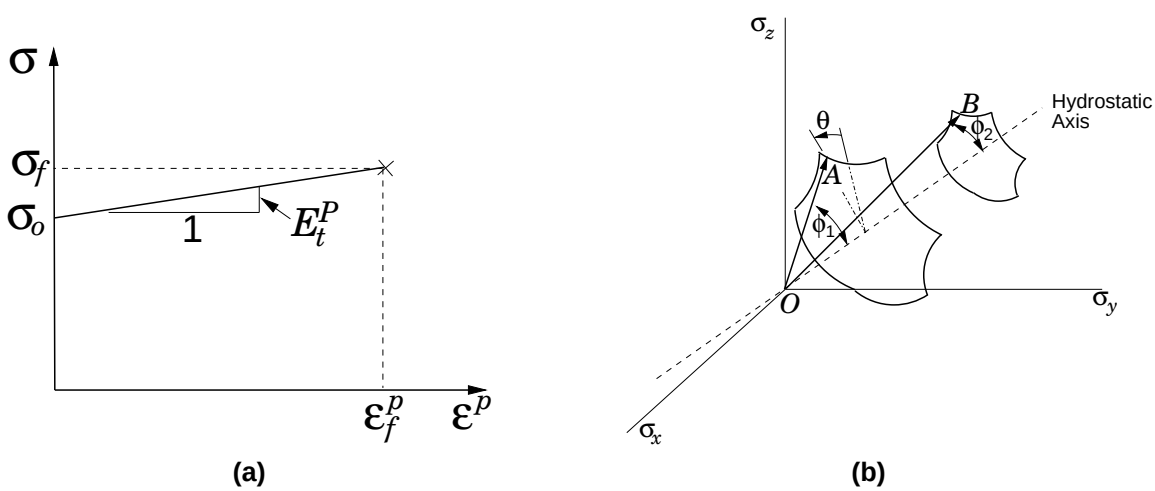

Figure 6: (a) Linear stress-plastic-strain curve with parameters and (b) schematic of failure contours in principal stress space.

The angle θ is the Lode angle and represents a rotation about the hydrostatic axis. Following a stress path with given ϕ and θ from the origin, the stress components will

eventually become high enough to satisfy a ductile failure criterion, thus generating a failure point in principal stress space. Considering paths with constant ϕ but different values of θ generates closed contours as shown in Fig. 6(b) for two values of ϕ. If the failure criterion is independent of the Lode angle θ, the contours will be circles. The lines shown are examples of a failure criterion that is Lode angle dependent. Note that the lines do not have to lie in a plane with constant hydrostatic stress. The shapes shown for ϕ_1 and ϕ_2 are drawn with different sizes to represent a failure criterion that is also dependent on triaxiality. A criterion that is triaxiality independent would produce shapes of equal size. In general, it is expected that the size of the failure contours would decrease with increasing triaxiality (decreasing ϕ) as mentioned in Section 1.1 and illustrated in Fig. 6(b).

One of two methods were used to generate the failure surface for each of the failure criteria considered.

Method A:

In this procedure a series of numerical calculations were performed where the stress magnitude was increased incrementally for constant values of ϕ and θ. At each increment, the plastic strains, the equivalent plastic strain, and other state variables were calculated using the relations presented in Section 2. With this information, a given failure criterion was evaluated until failure was detected. By changing the value of θ the failure contour at constant triaxiality was determined. Once this was performed, similar failure contours were generated for other values of ϕ. Finally, a failure envelope was generated by joining the different contours.

Method B:

Given the simplicity of the hardening function and of the stress history, it is also possible to obtain closed-form solutions for the stress at failure as follows. Suppose that we are following a proportional stress path with constant ϕ and θ. Decomposing the stress components as suggested by (6), we can write

$$\sigma_x = \sigma_m + s_x \tag{14a}$$

$$\sigma_y = \sigma_m + s_y \tag{14b}$$

$$\sigma_z = \sigma_m + s_z \tag{14c}$$

where the deviatoric stress components will be written as

$$s_x = s \tag{15a}$$

$$s_y = \alpha\, s \tag{15b}$$

$$s_z = -(1+\alpha)\, s. \tag{15c}$$

Note that $s_x + s_y + s_z = 0$ as required. All calculations conducted in Section 4 will be carried out with $s > 0$. Therefore, this condition is also assumed in the following development.

From (7) and (15) the equivalent stress is

$$\sigma_e = \sqrt{3(1+\alpha+\alpha^2)}\, s \tag{16}$$

Since first yield occurs when $\sigma_e = \sigma_o$, the value of s at yield is given by

$$\bar{s}_o = \frac{\sigma_o}{\sqrt{3(1+\alpha+\alpha^2)}}. \tag{17}$$

From (13), constant ϕ implies constant η. Then from (17) and (8), the relation between σ_m and η is

$$\sigma_m = \eta\sqrt{3(1+\alpha+\alpha^2)}s. \tag{18}$$

The relation between θ and α depends on the range of α. The calculations presented in the next section will be conducted with $-1/2 \leq \alpha \leq 1$. In this range $\sigma_x > \sigma_y > \sigma_z$ and

$$\sqrt{3}\tan\theta = \frac{2\sigma_y - \sigma_x - \sigma_z}{\sigma_x - \sigma_z}.$$

Combining with 14 and 15 gives

$$\tan\theta = \frac{\sqrt{3}\alpha}{2+\alpha}. \tag{19}$$

From (12) the plastic strain increments are

$$\mathrm{d}\varepsilon_x^p = \frac{3}{2}\frac{\mathrm{d}s}{E_t^p} \tag{20a}$$

$$\mathrm{d}\varepsilon_y^p = \alpha \mathrm{d}\varepsilon_x \tag{20b}$$

$$\mathrm{d}\varepsilon_y^p = -(1+\alpha)\mathrm{d}\varepsilon_x. \tag{20c}$$

Integrating for constant E_t^p and α gives

$$\varepsilon_x^p = \frac{3}{2}\frac{s-\bar{s}_o}{E_t^p} \tag{21a}$$

$$\varepsilon_y^p = \alpha\varepsilon_x \tag{21b}$$

$$\varepsilon_z^p = -(1+\alpha)\varepsilon_x. \tag{21c}$$

Finally, the expression for the equivalent plastic strain increment can be obtained by substituting (20) into (11), which gives

$$\mathrm{d}\varepsilon_e^p = \sqrt{3(1+\alpha+\alpha^2)}\,\frac{\mathrm{d}s}{E_t^p}, \tag{22}$$

and, integrating,

$$\varepsilon_e^p = \sqrt{3(1+\alpha+\alpha^2)}\,\frac{s-\bar{s}_o}{E_t^p} \tag{23}$$

Note that using (16) and (17) in (23) gives

$$\varepsilon_e^p = \frac{\sigma_e - \sigma_o}{E_t^p} \tag{24}$$

as can be seen in Fig. 6(a). Keep in mind that the equivalent stress-plastic-strain curve is the same as the uniaxial stress-plastic-strain curve.

3.2 Plane Stress

Plane stress in the x-y plane is defined as a state of stress having components $\sigma_{zz} = \sigma_{xz} = \sigma_{yz} = 0$. The principal stress has two non-zero normal components σ_x and σ_y, as shown in Fig. 7(b). The third principal component σ_z is zero at all times. As in Section 3.1, proportional stress loading was considered (see Fig. 7(c)) with $\sigma_x = \sigma$ and $\sigma_y = \beta\sigma_x$ for a material with constant hardening modulus as shown in Fig. 7(a). The same material properties used in the 3D examples were used for plane stress, and one of two methods were used to calculate each failure envelope.

Method A:

In this method, the stress components were incremented along proportional stress paths (constant values of ω, as defined in Fig. 7c), while calculating the plastic strain components and checking the failure criterion. Once the failure criterion was met, the stress and strain values were stored, and the process was repeated for a new value of ω. Finally, the stored variables for $-180° \leq \omega \leq 180°$ were assembled to generate the plane stress failure envelope.

Method B:

Since the failure criteria considered are isotropic, the failure envelopes will be symmetric about the line $\sigma_y = \sigma_x$ in Fig. 8(c). As a result, calculations need only be conducted in the regions labeled 1, 2 and 3. Each of the regions have the following characteristics:

Region 1: $\sigma > 0$, $0 \leq \beta \leq 1$, $\sigma_1 = \sigma_x$, $\sigma_2 = \sigma_y$ and $\sigma_3 = 0$.

Region 2: $\sigma > 0$, $-\infty \leq \beta \leq 0$, $\sigma_1 = \sigma_x$, $\sigma_2 = 0$ and $\sigma_3 = \sigma_y$.

Region 3: $\sigma < 0$, $1 \leq \beta \leq \infty$, $\sigma_1 = 0$, $\sigma_2 = \sigma_y$ and $\sigma_3 = \sigma_x$.

The mean hydrostatic stress is given by

$$\sigma_m = \frac{1+\beta}{3}\,\sigma \tag{25}$$

while the equivalent stress is

$$\sigma_e = \sqrt{1-\beta+\beta^2}\,|\sigma| \tag{26}$$

and the Lode angle is

$$\sqrt{3}\tan\theta = \begin{cases} 2\beta - 1, & \text{in region 1} \\ -\frac{1+\beta}{1-\beta}, & \text{in region 2} \\ -\frac{2-\beta}{\beta}, & \text{in region 3.} \end{cases} . \tag{27}$$

Note that while in three dimensions the Lode angle and the triaxiality are independent, the plane stress condition ties them. Writing triaxiality (η) in terms of the Lode parameter ($\mu = \sqrt{3}\tan\theta$) gives

$$\eta = \begin{cases} \frac{3+\mu}{3\sqrt{3+\mu^2}}, & \text{in region 1} \\ \frac{-2\mu}{3\sqrt{3+\mu^2}}, & \text{in region 2} \\ -\frac{3+\mu}{3\sqrt{3+\mu^2}}, & \text{in region 3.} \end{cases} . \tag{28}$$

Because of the constant plastic tangent modulus of the material and the proportional stress path used, the equations of J_2 flow plasticity can be easily integrated to give the following expressions for the plastic strains:

$$\varepsilon_x^P = \frac{2-\beta}{2}\frac{|\sigma| - \bar{\sigma}_o}{E_t^P}\text{sgn}(\sigma) \tag{29a}$$

$$\varepsilon_y^P = \frac{2\beta-1}{2}\frac{|\sigma| - \bar{\sigma}_o}{E_t^P}\text{sgn}(\sigma) \tag{29b}$$

$$\varepsilon_z^P = -\frac{1+\beta}{2}\frac{|\sigma| - \bar{\sigma}_o}{E_t^P}\text{sgn}(\sigma) \tag{29c}$$

where

$$\bar{\sigma}_o = \frac{\sigma_o}{\sqrt{1-\beta+\beta^2}}. \tag{30}$$

is the value of σ at yield. The expression for the equivalent plastic strain is

$$\varepsilon_e^P = \sqrt{1-\beta+\beta^2}\,\frac{|\sigma| - \bar{\sigma}_o}{E_t^P}. \tag{31}$$

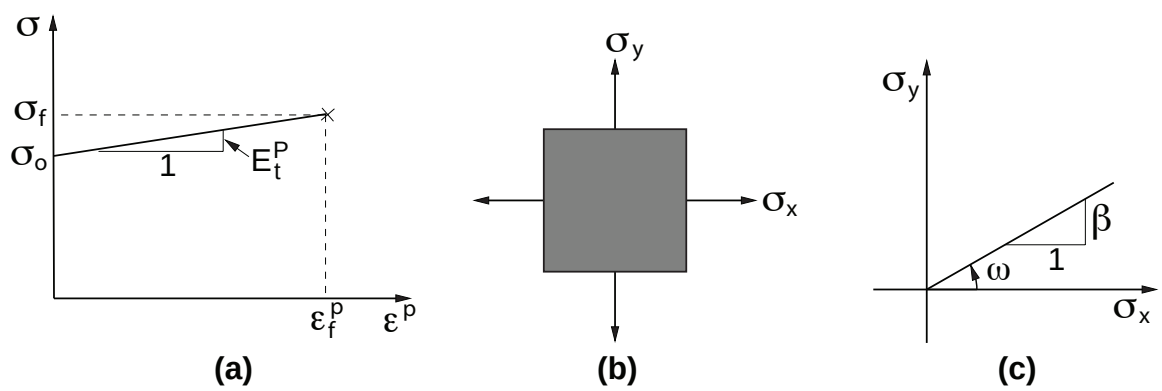

Figure 7: Definition of plane stress example parameters. (a) Stress-strain relationship parameters, (b) plane stress condition and (c) radial stress path.

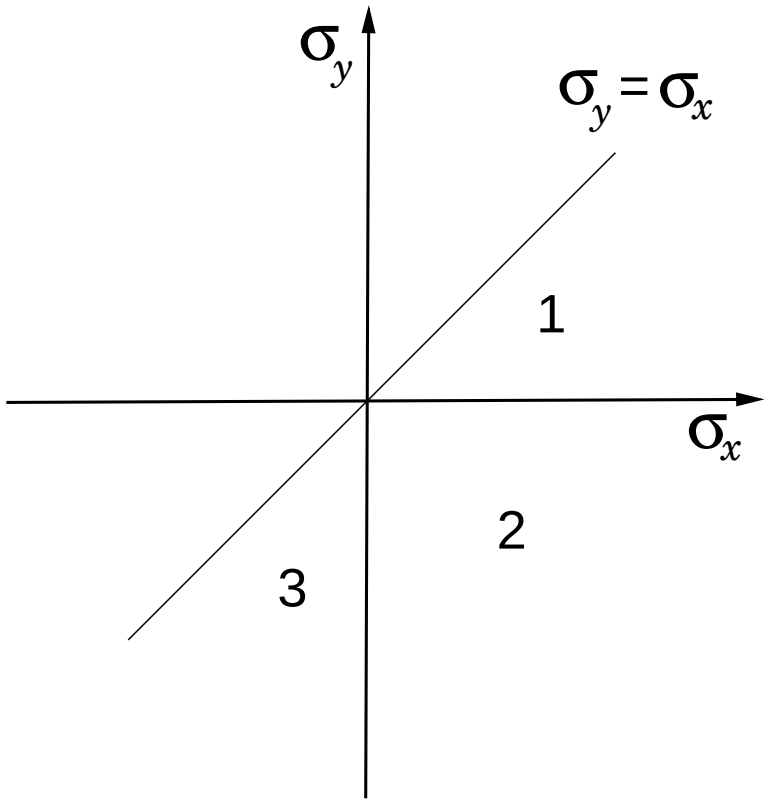

Figure 8: Plane stress space showing three regions where calculations will be conducted.

4 Failure Criteria

The next sections will first present examples of the failure contours in principal stress and strain spaces for various commonly used failure criteria using the proportional stress paths discussed previously. Following this, examples will be given of failure surfaces in principal stress space and how they project onto plane stress. Finally, the plane stress representation of each failure criterion will be discussed in detail. In all cases to be shown, the material parameters were taken as $\sigma_0 = 60$ ksi, $E_t^p = 1 \times 10^2$ ksi and $\varepsilon_f^p = 0.15$.

4.1 Equivalent Plastic Strain

Definition

Although it is not supported strongly by experimental data, the equivalent plastic strain failure criterion is the simplest and therefore one of the most widely used failure criteria. It is available in Abaqus as well as in Sierra/SM. The criterion states that failure at a material point occurs when the equivalent plastic strain reaches a failure value. In other words, when

$$\varepsilon_e^p = \varepsilon_f^p. \tag{32}$$

Here ε_f^p is the plastic strain at failure, and it is the only parameter that needs to be calibrated from test data. The most common calibration test is the uniaxial tension test, but others such as pure shear tests may also be used. In J_2 plasticity, the equivalent plastic strain is calculated incrementally as given in (11) and accumulates during plastic deformation. Therefore,

$$\varepsilon_e^p = \int \mathrm{d}\varepsilon_e^p = \int \sqrt{\frac{2}{3} d\varepsilon_{ij}^p \mathrm{d}\varepsilon_{ij}^p}. \tag{33}$$

Examples of Use

Documented examples of the use of this failure criterion include the Newton aircraft vulnerability project conducted at Sandia, Los Alamos and Lawrence Livermore National Laboratories (Alves *et al* (2012)). Validation studies on the failure of round thin-walled plates subjected to blast loading gave predictions that underestimated the explosive amount required to fail the plates. An increase of 20% in the value of ε_f^p determined from uniaxial tension tests was required to match the experimental data. This may indicate a deficiency in the failure criterion and/or the calibration procedure used in the uniaxial tension tests.

Another example was presented by Kazemahvazi *et al* (2007) who investigated the failure of circular copper plates subjected to an underwater shock. They reported calibration of the equivalent plastic strain at failure based on uniaxial tension tests. They took the failure strain to correspond to the plastic strain at which the ultimate tensile stress occurred. The

authors reported mesh dependency of the failure results and chose a mesh size to "ensure agreement with experimentally observed failure modes over the entire range of pressures investigated." The results indicated a tendency for the loads required to induce failure of the plates to be underestimated by about 20% in some cases.

Proportional Stress Paths–Three Dimensional Results

Using (24), setting $\varepsilon_e^p = \varepsilon_f^p$ and solving for the corresponding critical value of equivalent stress σ_{ec} gives

$$\sigma_{ec} = E_t^p \varepsilon_f^p + \sigma_o = \sigma_f.$$

Here, σ_f is the failure stress that corresponds to the specified plastic strain ε_f^p under uniaxial loading. This equation reveals that the equivalent plastic strain failure criterion is independent of both triaxiality and Lode angle. Hence, the single contour shown in Fig. 9(a) represents the failure criterion. The perspective shown is as if one was looking down the hydrostatic axis. The radius of the failure surface is $\sqrt{2/3}\ \sigma_f$ as shown in the figure. The initial yield surface is shown in green in the figure for reference. Figure 9(b) shows the corresponding contour of plastic strain on the π-plane, which is also a circle of radius $\sqrt{3/2}\varepsilon_f^p$.

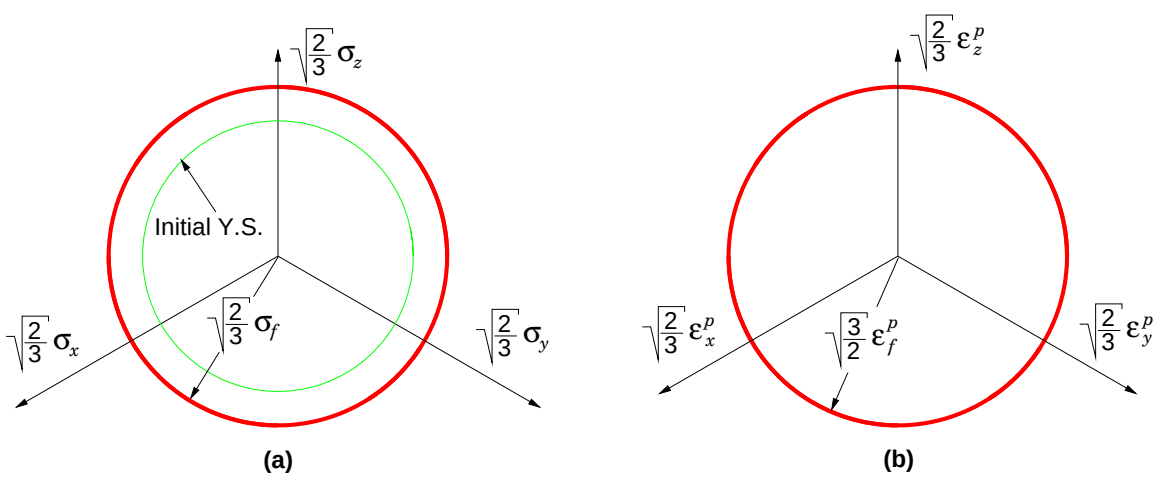

Figure 9: Stress and plastic strain states at failure according to the equivalent plastic strain failure criterion for 3D proportional stress paths. (a) Stress space and (b) plastic strain space.

Figure 10 shows a three-dimensional representation of the failure surface in principal stress space. It is simply a cylinder of circular cross-section with its axis aligned with he hydrostatic axis. The surface was plotted in a semi-transparent fashion, so the darker region represents the overlap of the front and back portions of the surface. The green line is the hydrostatic axis $\sigma_x = \sigma_y = \sigma_z$, whereas the red triad represents the principal stress axes passing through the origin. The intersection of the failure surface with a plane where one of the principal stresses is zero represents the case of plane stress and is of particular interest in the analysis of thin-walled structures. The black line in the figure shows the intersection

of the failure surface with the σ_x-σ_y plane and illustrates the shape of the failure surface in plane stress.

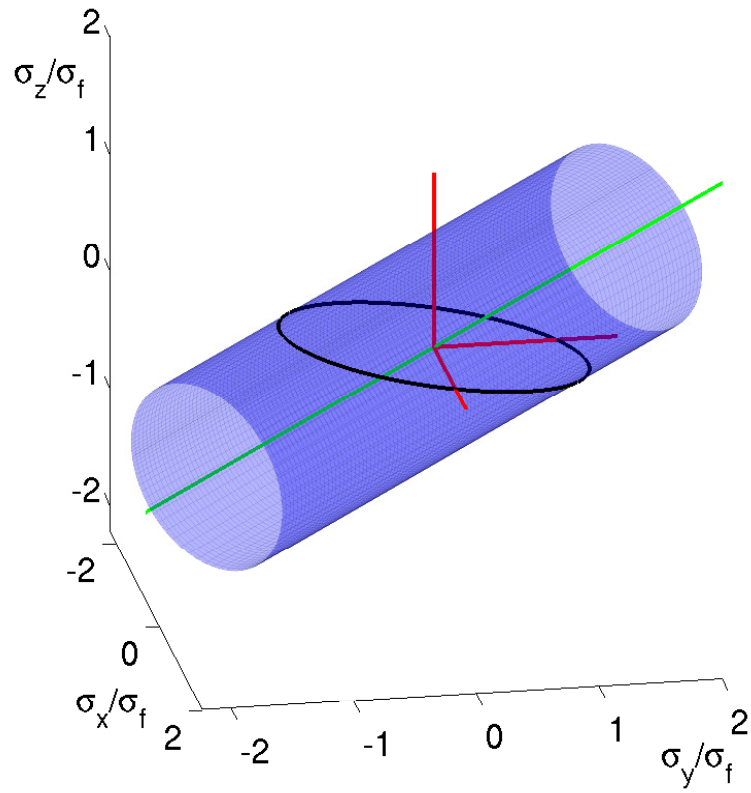

Figure 10: The equivalent plastic strain failure surface in principal stress space for 3D proportional stress paths. The hydrostatic axis is shown in green and the origin is shown by the intersection of the three red axes. The black line is the intersection with the σ_x-σ_y plane.

Proportional Stress Paths–Plane Stress Results

Figure 11(a) shows the calculated failure envelope in stress space for the case of plane stress. These were calculated using the plane stress relations presented in Section 3.2. Four symbols are included to identify particular states of stress. Equibiaxial tension ($\beta = 1$) is shown by the up triangle, "plane plastic strain," defined by $\varepsilon_y^p = 0$ ($\beta = 1/2$) is shown by the down triangle, uniaxial tension ($\beta = 0$) is shown by the square and pure shear ($\beta = -1$) is shown by the circle. Both stress components have been normalized by σ_f. As expected, the failure envelope has the shape of a von Mises ellipse. The initial yield surface is also included in green line as reference.

Figure 11(b) shows the corresponding in-plane plastic strain envelope while Fig. 11(c) shows the dependence of the critical equivalent plastic strain at failure (ε_{ec}^p) on the stress

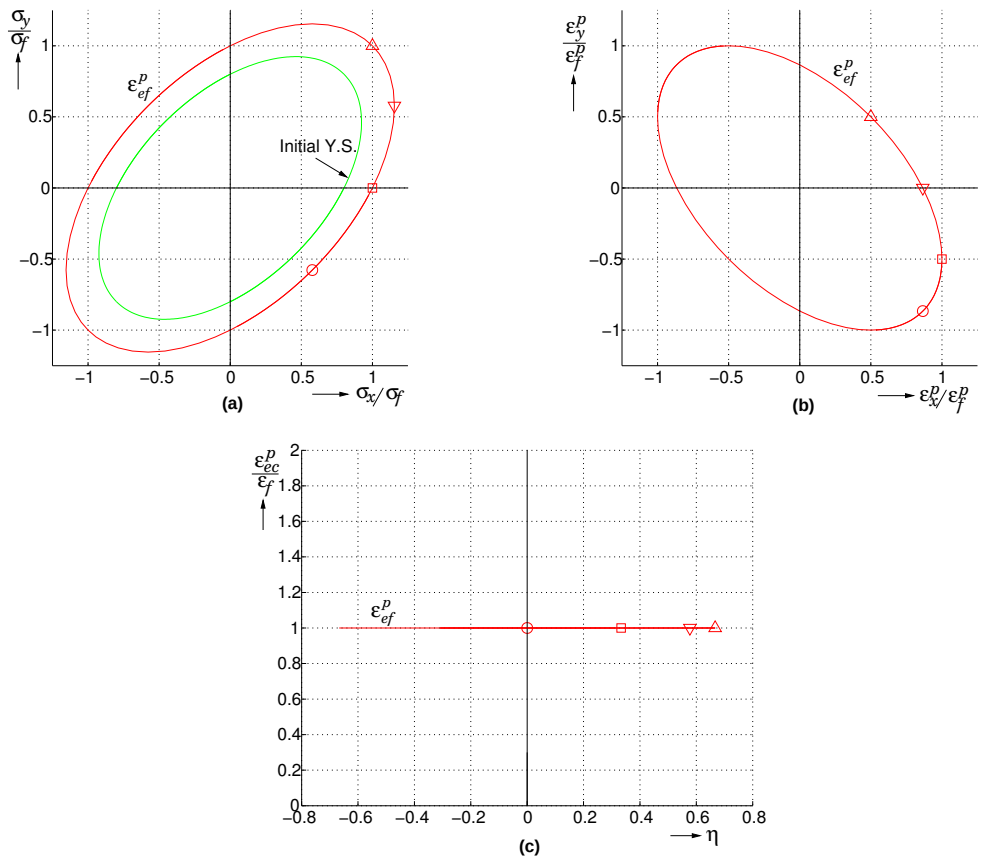

Figure 11: Equivalent plastic strain failure criterion for plane stress, proportional stress paths. (a) Stress space, (b) in-plane plastic strain space and (c) critical equivalent plastic strain vs. stress triaxiality.

triaxiality (η). As dictated by the definition of this failure criterion $\varepsilon^p_{ec} = \varepsilon^p_f$. It is important to note that because this failure criterion does not distinguish between states of stress with positive or negative triaxiality, the equivalent plastic strain to failure is the same whether the hydrostatic mean stress is positive or negative. Therefore, when used in problems with high compressive hydrostatic stress it predicts unexpected failure modes for triaxiality values near zero or negative, as has been demonstrated for plate puncture problems by Teng and Wierzbicki (2006).

4.2 Equivalent Plastic Strain in Tension

Definition

A simple modification to the equivalent plastic strain failure criterion to prevent failure under hydrostatic compression has been implemented in Sierra/SM by calculating a variable ε^p_{et}

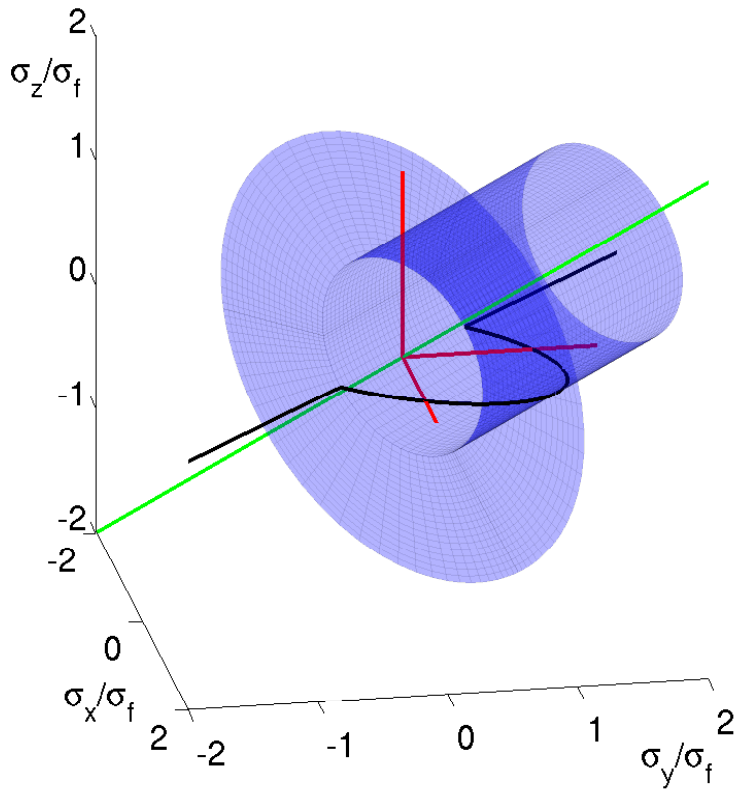

Figure 12: The equivalent plastic strain in tension failure surface in principal stress space for 3D proportional stress paths. The hydrostatic axis is shown in green and the origin is shown by the intersection of the three red axes. The black line is the intersection with the σ_x-σ_y plane.

called 'tensile_eqps' defined in incremental form as follows (Crane (2013)):

$$d\varepsilon^p_{et} = \begin{cases} d\varepsilon^p_e, \text{ if } \sigma_m > 0 \\ 0, \text{ if } \sigma_m \leq 0 \end{cases} . \tag{34}$$

In other words, the increment of equivalent plastic strain in tension only accumulates when the hydrostatic mean stress is positive. Failure is predicted to occur when

$$\varepsilon^p_{et} = \varepsilon^p_f. \tag{35}$$

As with the regular equivalent plastic strain criterion, only the parameter ε^p_f needs to be calibrated from test data. Note that this failure criterion is triaxiality dependent, but in a very simple and abrupt manner.

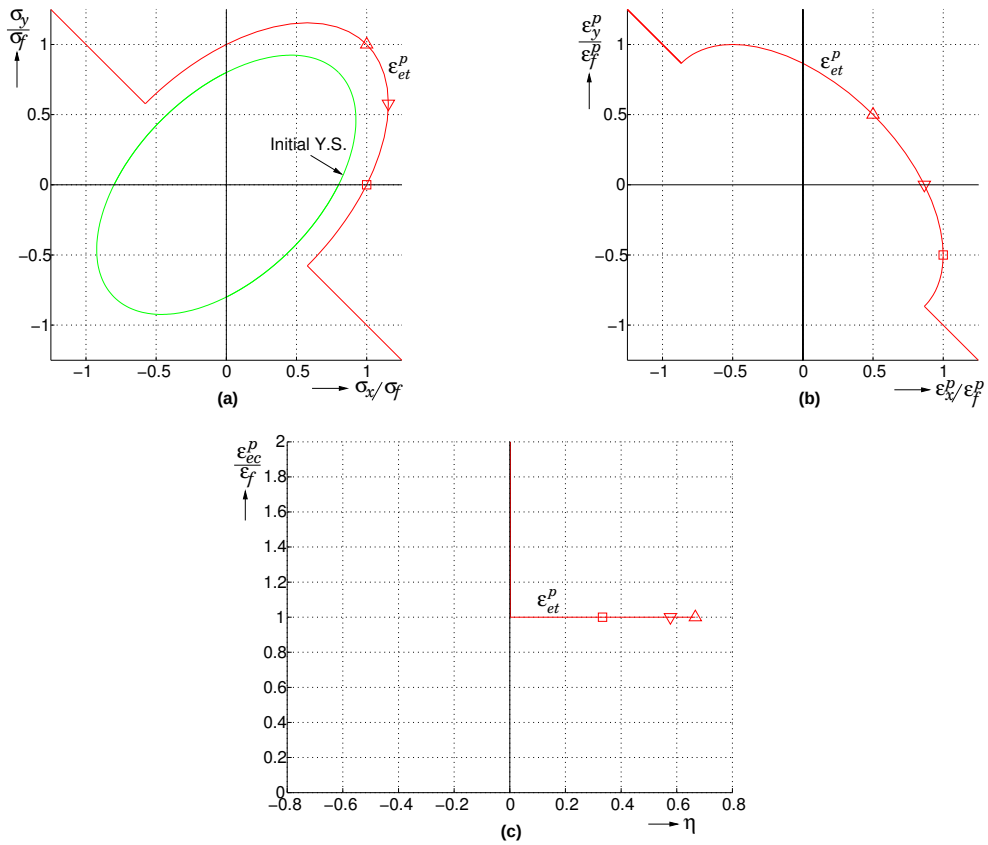

Figure 13: Equivalent plastic strain in tension failure criterion for plane stress, proportional stress paths. (a) Stress space, (b) in-plane plastic strain space, (c) critical equivalent plastic strain vs. stress triaxiality.

Examples of Use

This failure criterion was used for calculations in the Newton aircraft vulnerability project Alves *et al* (2012), but no direct comparison to experiment was reported. This criterion has also been used to prevent failure when the material is under negative triaxiality in other projects but, again, no record explicitly addressing the performance of this criterion has been found in a practical problem.

Proportional Stress Paths–Three Dimensional Results

Under proportional loading the failure contours produced by the equivalent plastic strain in tension criterion are identical to those of the equivalent plastic strain criterion as long as the stress triaxiality is positive. Therefore, the contours are identical to those shown in Fig. 9. Since no failure can occur for zero or negative triaxiality, one can think of the failure contours as having infinite radius under this condition. Figure 12 shows the three-dimensional failure prediction as a truncated cylinder whose radius goes to infinity at zero

triaxiality. The intersection of the failure surface with the σ_x-σ_y axis, shown in black line, consists of one-half of an ellipse as will be shown next in more detail.

Proportional Stress Paths–Plane Stress Results

The result of using this failure criterion under plane stress is presented in Fig. 13. The failure envelope in stress space is shown in Fig. 13(a) to be "open" over half of the second and fourth quadrants and the whole third quadrant. Therefore, no failure occurs for paths in those regions. The corresponding in-plane strain failure envelope is shown in Fig. 13(b). Figure 13(c) reflects exactly the definition of the failure criterion: failure occurs when $\varepsilon^p_{et} = \varepsilon^p_f$ if the triaxiality $\eta > 0$, and no failure occurs if $\eta \leq 0$.

4.3 Maximum Shear Stress

Definition

This is a simple stress-based criterion stating that failure occurs when the maximum shear stress reaches a prescribed value. The maximum shear stress can be easily calculated if the three principal stresses are known. If they are ordered such that $\sigma_1 > \sigma_2 > \sigma_3$ then the maximum shear stress, $\tau_{\max}$, is given by

$$\tau_{\max} = \frac{\sigma_1 - \sigma_3}{2}. \tag{36}$$

The material is taken to fail when

$$\tau_{\max} = \tau_f. \tag{37}$$

Here τ_f is the maximum shear stress at failure. As in the previous two cases, only a single parameter, the value of τ_f, needs to be calibrated from test data. Again, a simple uniaxial tension test is a possibility. For J_2 plasticity models, $\tau_f = \sigma_f/2$.

Examples of Use

This was one of the models evaluated in plane stress by Wierzbicki *et al* (2005) for states of stress with triaxialities $\eta > -1/3$. In their evaluation of seven failure models, they concluded that this simple model fit their experimental data very well and was therefore a "winner." Similarly, Vallellano *et al* (2007) found that this failure criterion fitted the measured biaxial strain failure data of Al 2024 sheet under stretch much better than other criteria.

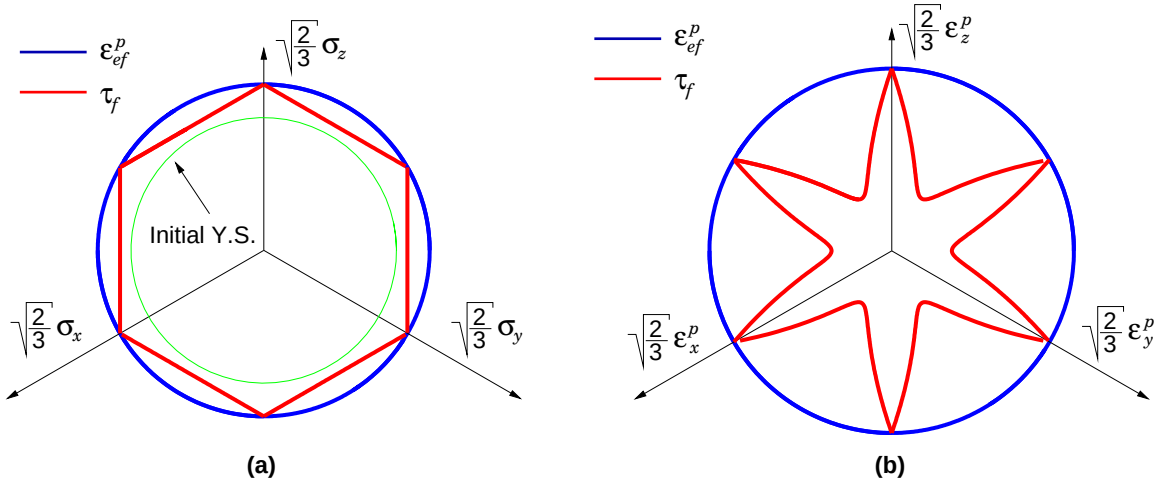

Figure 14: Stress and plastic strain states at failure according to the maximum shear stress failure criterion for 3D proportional stress paths. (a) Stress space and (b) plastic strain space.

Proportional Stress Paths–Three Dimensional Results

Since this failure criterion is completely defined in terms of stress we can easily determine the stresses at failure as follows. Consider the ranges of α and s in (15) to be $-1/2 \leq \alpha \leq 1$ and $s > 0$. In this range $\sigma_1 = \sigma_x$, $\sigma_2 = \sigma_y$ and $\sigma_3 = \sigma_z$. It covers the segment in the π-plane, shown in Fig. 5, that lies between the projection of the positive σ_x axis when $\alpha = -\frac{1}{2}$ and the projection of the negative σ_z axis when $\alpha = 1$. As mentioned in Section 3.2, this range covers one-sixth of the π-plane. For an isotropic failure criterion, five similar segments can be determined by reflection of the failure surface about the stress axes. The maximum shear stress in the segment of interest is given by

$$\tau_{\max} = \frac{2+\alpha}{2}\, s. \tag{38}$$

Note that $\tau_{\max}$ is independent of σ_m, so the maximum shear failure criterion does not depend on triaxiality. To find the critical value of s at failure (s_c), use (38) and solve for s_c, giving

$$s_c = \frac{2\tau_f}{2+\alpha} \tag{39}$$

The other stress components can the be found from (15), (14) and (18). As in the equivalent plastic strain criterion, a single contour, shown in Fig. 14(a) in red, represents the failure criterion for any value of triaxiality in stress space. The contour calculated for the equivalent plastic strain criterion, as well as the contour of the yield surface are shown for reference. Note that the maximum shear failure criterion is a hexagon, which implies a Lode angle dependence, and that it is inscribed in the circle representing the equivalent plastic strain criterion.

Once s_c is known, the value of the strain components at failure can be found from (21). Figure 14(b) shows the comparison between the plastic strains at failure predicted by the

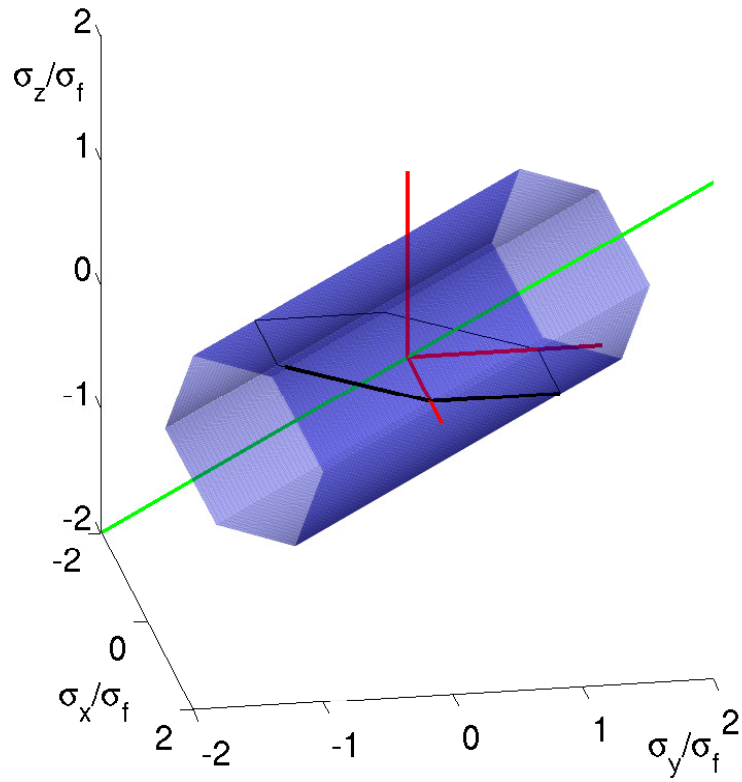

Figure 15: The maximum shear criterion failure surface in principal stress space for 3D proportional stress paths. The hydrostatic axis is shown in green and the origin is shown by the intersection of the three red axes. The black line is the intersection with the σ_x-σ_y plane.

maximum shear and equivalent plastic strain criteria. Note that in strain space, the criterion takes a "star" shape as shown. The reason for the star shape can be clearly seen in Fig. 14(a). Note that along certain directions the distance between the yield surface and the failure surface is smaller and gives the valleys in the star. Where the vertices occur in stress space, the results have to agree with those from the equivalent plastic strain failure criterion, thus giving the points of the star in strain space. So, clearly the combination of using J_2 plasticity and the maximum shear failure criterion results in the star shape of the plastic strain contours.

From (23) the value of the equivalent plastic strain at failure is given by

$$\varepsilon^p_{ec} = \sqrt{3(1+\alpha+\alpha^2)}\frac{\frac{2\tau_f}{2+\alpha} - \bar{s}_o}{E^p_t}. \tag{40}$$

So, while ε^p_{ec} depends on α and therefore on the Lode angle θ, it does not depend on triaxiality.

The three-dimensional representation of the failure surface is shown in Fig. 15 together with its intersection with the σ_x-σ_y plane.

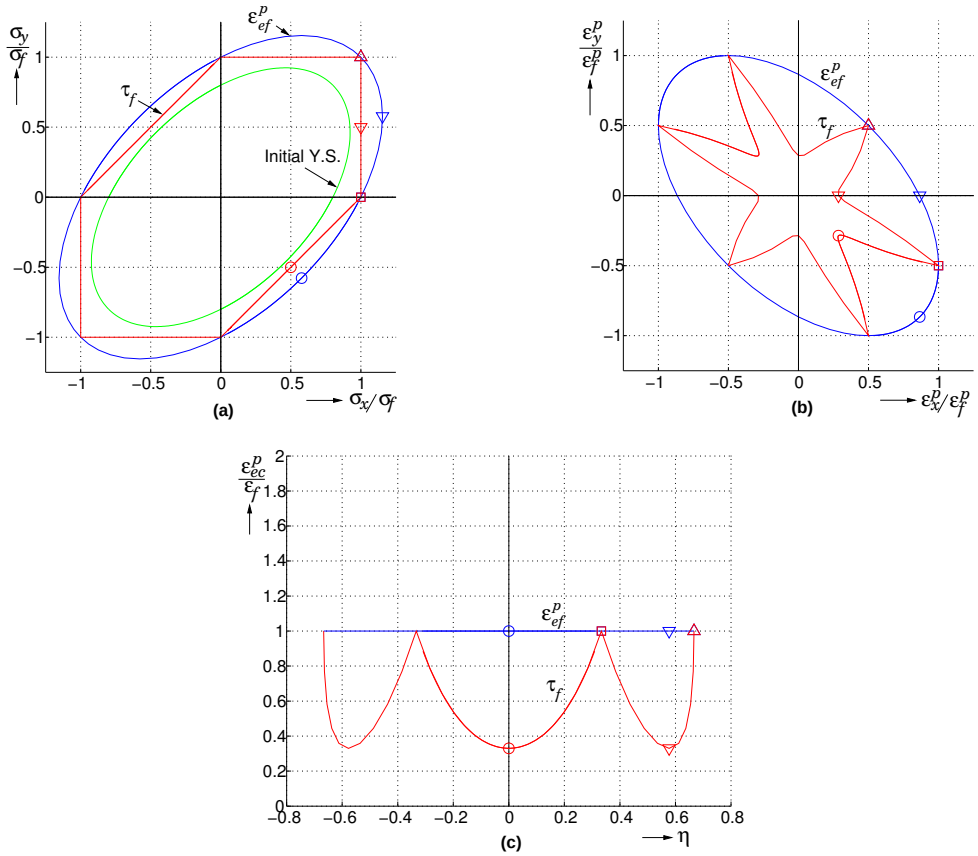

Figure 16: Maximum shear stress failure criterion for plane stress, proportional stress paths. (a) Stress space, (b) in-plane plastic strain space and (c) critical equivalent plastic strain vs. stress triaxiality. The results from the equivalent plastic strain criterion are shown for reference in blue line.

Proportional Stress Paths–Plane Stress Results

In the case of plane stress, the maximum shear stress is given by

$$\tau_{\max} = \begin{cases} \frac{\sigma}{2}, \text{ if } \sigma > 0 \text{ and } 0 \leq \beta \leq 1 \\ \frac{1-\beta}{2}\,\sigma, \text{ if } \sigma > 0 \text{ and } -\infty \leq \beta \leq 0 \\ -\frac{\beta\sigma}{2}, \text{ if } \sigma < 0 \text{ and } 1 \leq \beta \leq \infty. \end{cases} \tag{41}$$

The plane stress failure envelopes are shown in Fig. 16 in red line. The results obtained for the equivalent plastic strain criterion are shown in blue for comparison. The failure envelope in terms of the stress is shown in Fig. 16(a). As previously seen, this envelope has the shape of the Tresca hexagon in plane stress. The largest differences between the two criteria occur for the cases of "plane plastic strain" and pure shear. Although the differences may seem small in stress space, they become quite dramatic when looking at the in-plane plastic strain space as seen in Fig. 16(b). A shallow plastic tangent modulus projects a small stress

difference into a large plastic strain difference. The critical values of equivalent plastic strain as a function of stress triaxiality are shown in Fig. 16(c). Clearly, the critical equivalent plastic strain varies considerably. The material is most ductile under uniaxial loading and under balanced biaxial loading and least ductile under pure shear and "plane plastic strain" conditions. Recall, however, that this failure criterion is triaxiality independent but Lode angle dependent. It was previously discussed that in plane stress the triaxialty and the Lode angle are related by (28). Hence, the trend shown in Fig. 16(c) is a reflection of Lode angle dependence rather than triaxiality dependence.

This failure criterion does not distinguish between states of stress with positive or negative triaxiality. As a result, it suffers from the same deficiencies as the equivalent plastic strain criterion when states of stress with high compressive mean stresses are present.

4.4 Mohr-Coulomb

Definition

The Mohr-Coulomb failure model has its roots in the field of geomechanics. In a recent paper Bai and Wierzbicki (2010) proposed the use of this model for ductile fracture because it exhibits both triaxiality and Lode angle dependence. Their observations that both of these parameters are important in the prediction of ductile fracture motivated their consideration of this model.

The Mohr-Coulomb failure criterion is given by the expression

$$M = \tau + c_1 \sigma_n = c_2 \tag{42}$$

where τ and σ_n are the shear and normal traction components, given by (2) and (3) on a plane that maximizes M. The parameters c_1 and c_2 are material constants. Note that if $c_1 = 0$, the criterion reduces to the maximum shear stress criterion. Bai and Wierzbicki have shown that by maximizing M with respect to the plane orientation, the criterion reduces to

$$\frac{1}{2}\left[\left(\sqrt{1+c_1^2}+c_1\right)\sigma_1 - \left(\sqrt{1+c_1^2}-c_1\right)\sigma_3\right] = c_2. \tag{43}$$

Recall that the principal stresses have been ordered such that $\sigma_1 \geq \sigma_2 \geq \sigma_3$.

Examples of Use

This criterion has been used extensively for concrete and geomaterials, but its use for ductile failure seems to have started with the papers by Bai and Wierzbicki (2010) and Beese *et al* (2010). Since then it has been used in the prediction of fracture in sheet metal by several investigators with reportedly reasonably good results. See, for example, the papers by Li *et al* (2010), Dunand and Mohr (2011) and Ebnoether and Mohr (2013). In some of these

papers the criterion is modified and is generally used in conjunction with plasticity models that are more sophisticated than the one used in this work.

Proportional Stress Paths–Three Dimensional Results

The Mohr-Coulomb failure criterion is, like the maximum shear criterion, stress-based. As was done when considering maximum shear, the range $-1/2 \leq \alpha \leq 1$ and $s > 0$ will be considered in (15). Recall that in this range, $\sigma_1 = \sigma_x$ and $\sigma_3 = \sigma_z$. Substituting from (14) and (15) into (43) yields the relation for s_c as follows

$$s_c = \frac{c_2 - c_1 \sigma_m}{k}$$

where

$$k = \left[\sqrt{1 + c_1^2} + \frac{1}{2} \left(\sqrt{1 + c_1^2} - c_1 \right) \alpha \right].$$

Using (8) to write the triaxiality η instead of σ_m above and using (16) gives the final expression for the critical value at failure

$$s_c = \frac{c_2}{\left[k + c_1 \eta \sqrt{3\left(1 + \alpha + \alpha^2\right)} \right]}. \tag{44}$$

It is then clear that this failure criterion depends on both the triaxiality and the Lode angle, and that the values of c_1 and c_2 need to be calibrated from experimental data. Our simple example requires that, under uniaxial stress conditions, failure occur when the plastic strain reaches the value ε_f, which corresponds to a stress σ_f. Substituting $\sigma_1 = \sigma_f$ and $\sigma_3 = 0$ in (43) yields a relation between c_1 and c_2 as follows

$$\frac{1}{2} \left(\sqrt{1 + c_1^2} + c_1 \right) \sigma_f = c_2. \tag{45}$$

Therefore, only the value of c_1 will be prescribed in the examples that follow. The value of c_2 will be determined from (45).

Once s_c is determined from (44), the rest of the stress components can be found from (15) and (14). Examples of failure contours for four values of triaxiality are shown in Figs. 17(a) and (c) for $c_1 = 0.2$ and 0.4 respectively. The results show that the shapes of the failure contours resemble a distorted hexagon. The effect of triaxiality is enhanced as c_1 increases. The case with $c_1 = 0$ is not shown but, as indicated previously, it is equivalent to the maximum shear failure criterion shown in Fig. 14(a). Comparing the stress contours in Fig. 14(a) to those in Figs. 17(a) and (c) shows that the distortion of the maximum shear stress hexagon increases with c_1. The results also show that for sufficiently high triaxialities, parts or the whole failure contour can be inside the yield surface. Presumably, in theses cases failure would be declared upon yielding. Finally, note that failure is asymmetric with respect to the positive and negative uniaxial stress directions.

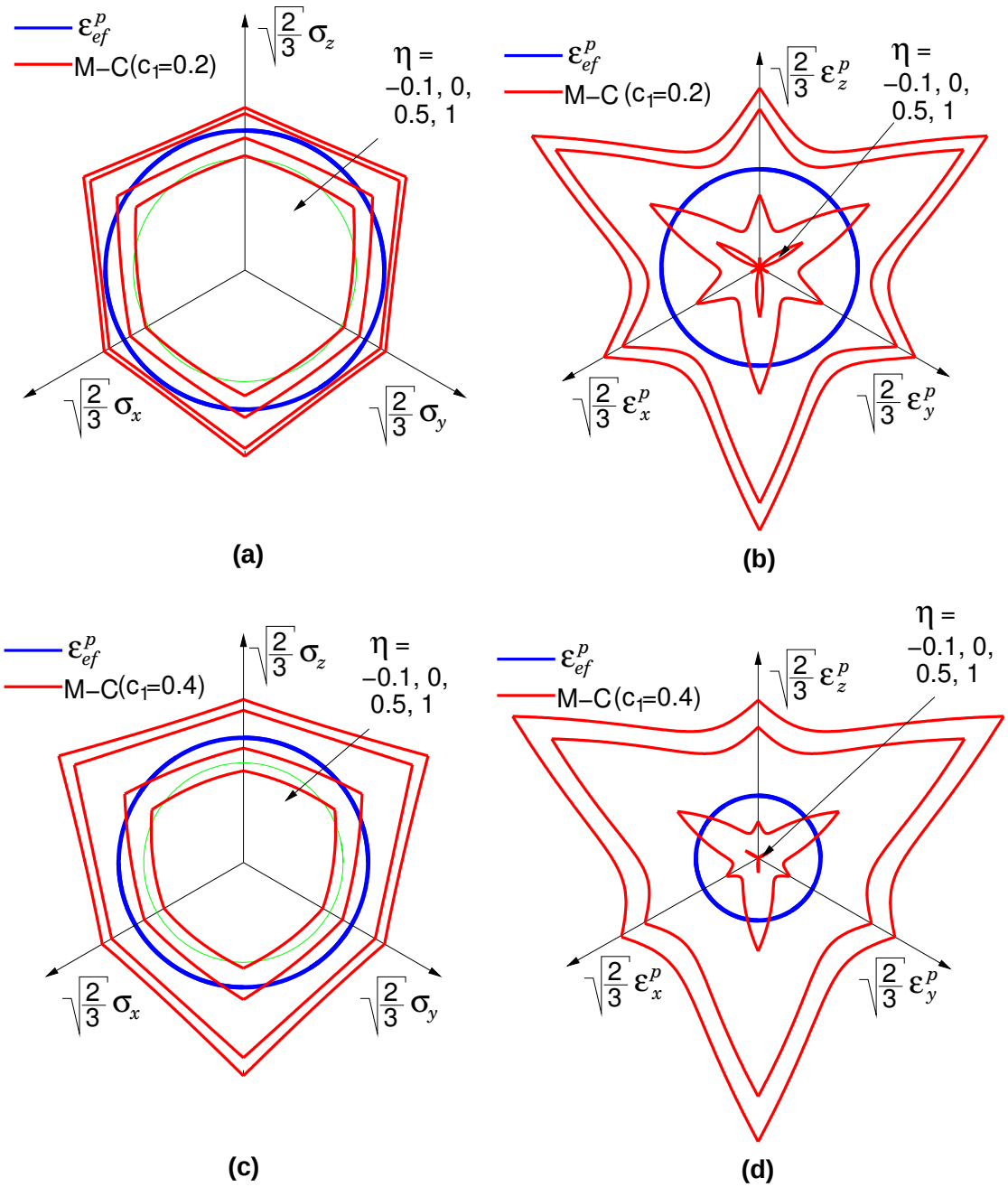

Figure 17: Stress and plastic strain states at failure according to the Mohr-Coulomb failure criterion for 3D proportional stress paths. (a) Stress space, $c_1 = 0.2$, (b) plastic strain space, $c_1 = 0.2$, (c) stress space, $c_1 = 0.4$ and (d) plastic strain space, $c_1 = 0.4$.

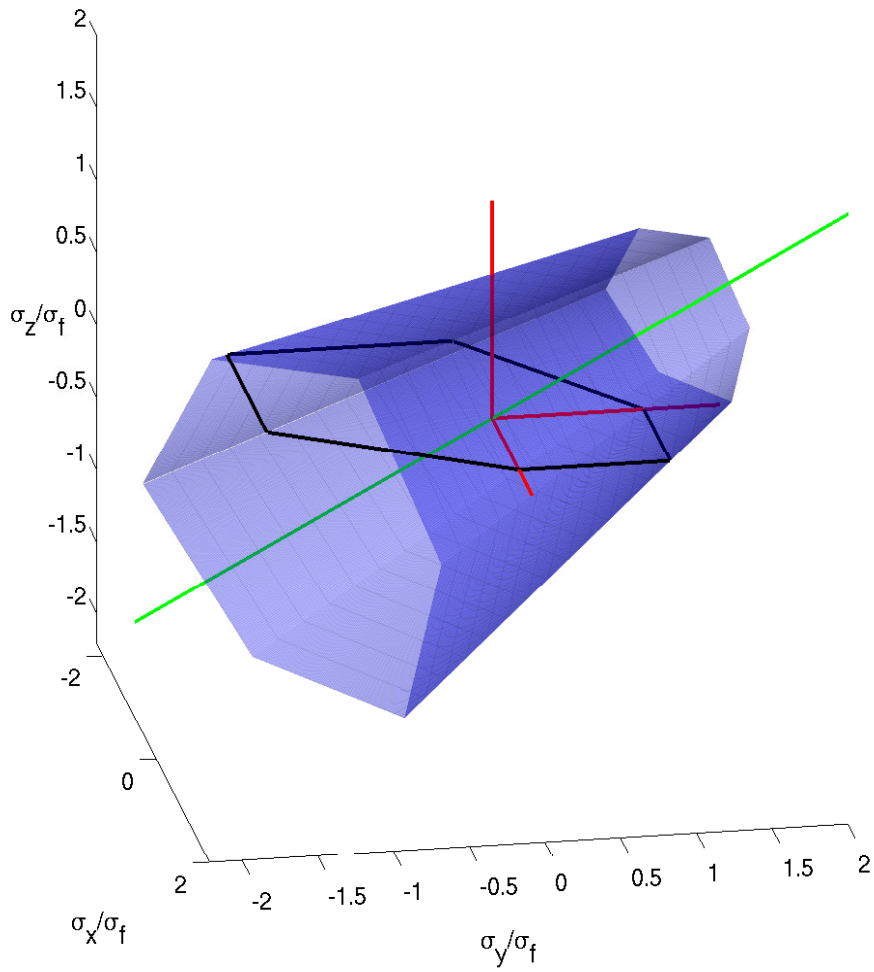

Figure 18: The Mohr-Coulomb failure surface in principal stress space for 3D proportional stress paths ($c_1 = 0.2$). The hydrostatic axis is shown in green and the origin is shown by the intersection of the three red axes. The black line is the intersection with the σ_x-σ_y plane.

The strains at failure are found from (21) and produce the contours shown in Figs. 17(b) and (d) for $c_1 = 0.2$ and 0.4. As expected the contours have 'star' shapes like the maximum shear criterion, but with distortions that increase with c_1. The equivalent plastic strain at failure can be found by substituting (44) into (23). Clearly ε^p_{ec} depends on both the Lode angle θ and triaxiality η.

The three-dimensional representation of the failure surface for $c_1 = 0.2$ is shown in Fig. 18, together with its intersection with the σ_x-σ_y plane that constitutes the plane stress failure contour that will be discussed next.

Proportional Stress Paths–Plane Stress Results

In the case of plane stress, tracing the failure contours requires splitting the calculations into three parts as indicated in Section 3.2. The expressions for the critical value σ_c are as follows:

$$\sigma_c = \begin{cases} \sigma_f, \text{ if } \sigma > 0 \text{ and } 0 \leq \beta \leq 1 \\ \frac{\left(\sqrt{1+c_1^2}+c_1\right)\sigma_f}{\sqrt{1+c_1^2}+c_1-\left(\sqrt{1+c_1^2}-c_1\right)\beta}, \text{ if } \sigma > 0 \text{ and } -\infty \leq \beta \leq 0 \\ -\frac{\sqrt{1+c_1^2}+c_1}{\sqrt{1+c_1^2}-c_1}\frac{\sigma_f}{\beta}, \text{ if } \sigma < 0 \text{ and } 1 \leq \beta \leq \infty \end{cases} . \tag{46}$$

These equations produce one-half of the envelope, and the other half can be obtained by reflection about the $\sigma_x = sigma_y$ line.

The results for the stress contours are shown in Fig. 19(a) in red line, together with the results from the equivalent plastic strain criterion shown in blue. Note that all the stress contours are closed and that the segment in the first quadrant is independent of c_1. The plastic strains at failure, obtained with (29) are shown in Fig. 19(b) while the equivalent plastic strain at failure obtained from (31) is shown in Fig. 19(c). As indicated previously, the results differ more and more from those of the maximum shear criterion as c_1 increases.

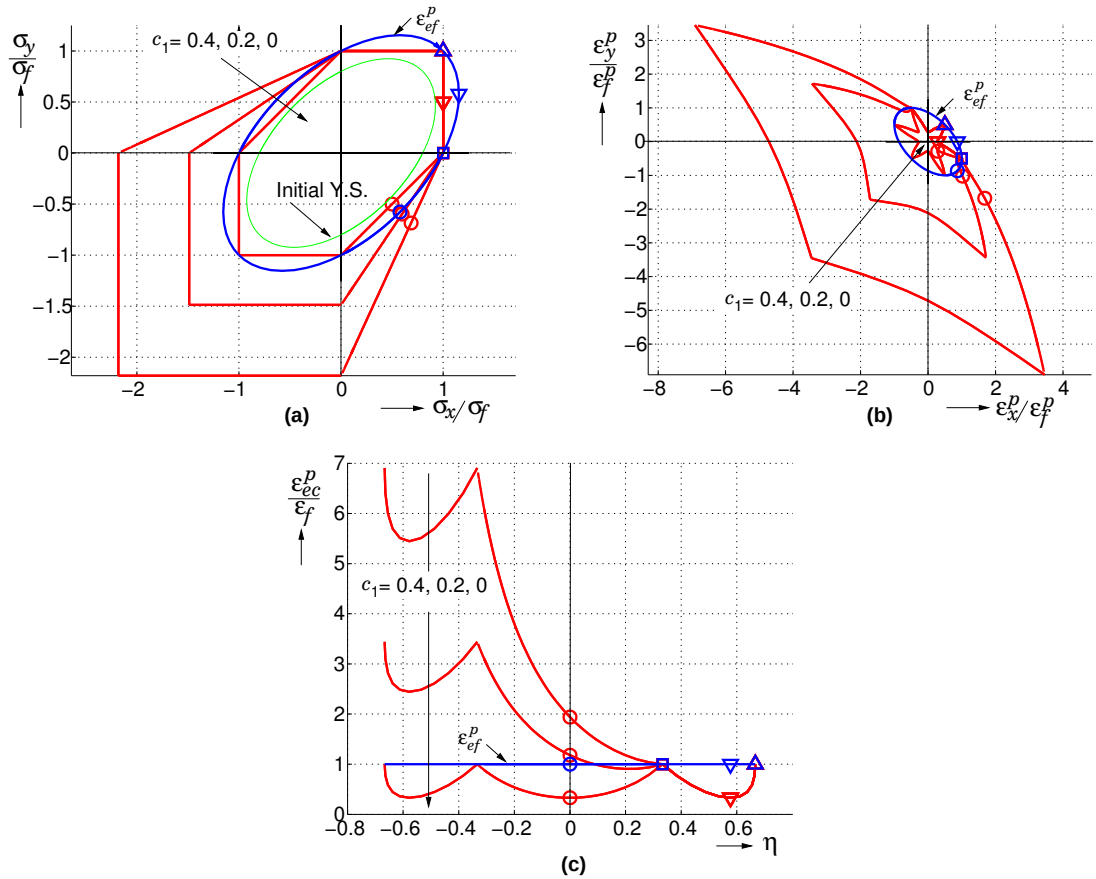

Figure 19: Mohr-Coulomb failure criterion for plane stress, proportional stress paths. (a) Stress space, (b) in-plane plastic strain space, (c) critical equivalent plastic strain vs. stress triaxiality. The results from the equivalent plastic strain criterion are shown for reference in blue line.

4.5 Tearing Parameter

Definition

The tearing parameter is a simple, empirical ductile failure model that is currently implemented in Sierra/SM as part of the Multi-Linear Elastic-Plastic (MLEP) with failure plasticity model. The MLEP model is a classical iso-thermal and rate independent J_2 plasticity model. Although it provides a choice of isotropic and kinematic hardening, only the isotropic hardening option is regularly used at SNL. The failure model is a modification of that originally proposed by Brozzo *et al* (1972). This model was evaluated and compared against other failure criteria by Wellman and Salzbrenner (1992). Subsequently, Wellman adopted it, modified it and implemented it in Sierra/SM (Wellman, 2012). In the current form implemented in Sierra Solid Mechanics Team (2013), the expression for the tearing

parameter is given by

$$\psi = \int_0^{\varepsilon_e^p} \left\langle \frac{2\sigma_1}{3(\sigma_1 - \sigma_m)} \right\rangle^{\xi} \mathrm{d}\hat{\varepsilon}_e^p, \tag{47}$$

where ε_e^p is the equivalent plastic strain, σ_1 is the largest principal stress, σ_m is the hydrostatic mean stress and ξ is a parameter. Clearly, this criterion exhibits dependence on mean stress and hence triaxiality. The Macaulay bracket is interpreted as

$$\langle a \rangle = \begin{cases} a, & \text{if } a > 0 \\ 0, & \text{if } a \leq 0. \end{cases}$$

Failure occurs when

$$\psi = \psi_f \tag{48}$$

where ψ_f is the value of the tearing parameter at failure. Note that under uniaxial conditions with $\sigma_1 = \sigma$ and $\sigma_2 = \sigma_3 = 0$ (47) gives $\psi = \varepsilon_e^p$. Hence, setting $\psi_f = \varepsilon_f^p$ gives failure when the uniaxial plastic strain is ε_f^p.

Using the tearing parameter failure criterion requires data to calibrate two parameters: ψ_f and ξ. Wellman (2012) suggested setting $\xi = 4$ based on calibrations that he conducted using notched Al 6061-T6 specimens tested under tensile load. More recently, however, it has been found that using $\xi = 4$ does not fit the response of other materials well, so it is useful to make ξ a parameter to be calibrated based on test data.

Examples of Use

The tearing parameter failure criterion has been used often at SNL to make predictions of ductile failure in various applications with varying degree of success. Most of the usage of this failure criterion seems to be included in various internal Sandia memos and a few SAND reports. The objective of the initial evaluation conducted by Wellman and Salzbrenner (1992) was to model the punching of exclusion barrier mock-ups. Since then, this failure criterion has been applied to other problems.

Prior to about the year 2000, the value of ξ used in most analyses was one, which is in agreement with the original model by Brozzo *et al* (1972). Starting around 1998, however, the value of ξ was changed to four to achieve better agreement with experimental failure measurements conducted on Al 6061-T6 notched specimens. Wellman (2012) indicated that the tearing parameter "has been used with many materials with a good degree of success," but acknowledged that for less ductile metals, such as Al 2024-T3, the predictions were not accurate. He also identified shear loading as another source of concern. It has been known that using the tearing parameter gives responses that are very tough in the vicinity of stress states where shear dominates. This may be improved by using smaller values of ξ as will be shown. The tearing parameter was used in the calculations of Al 7075 plate and cylinder puncture by Corona *et al* (2012). The results obtained with $\xi = 4$ overestimated the minimum punch-through velocity by about 60%. Given that in recent Sierra/SM releases

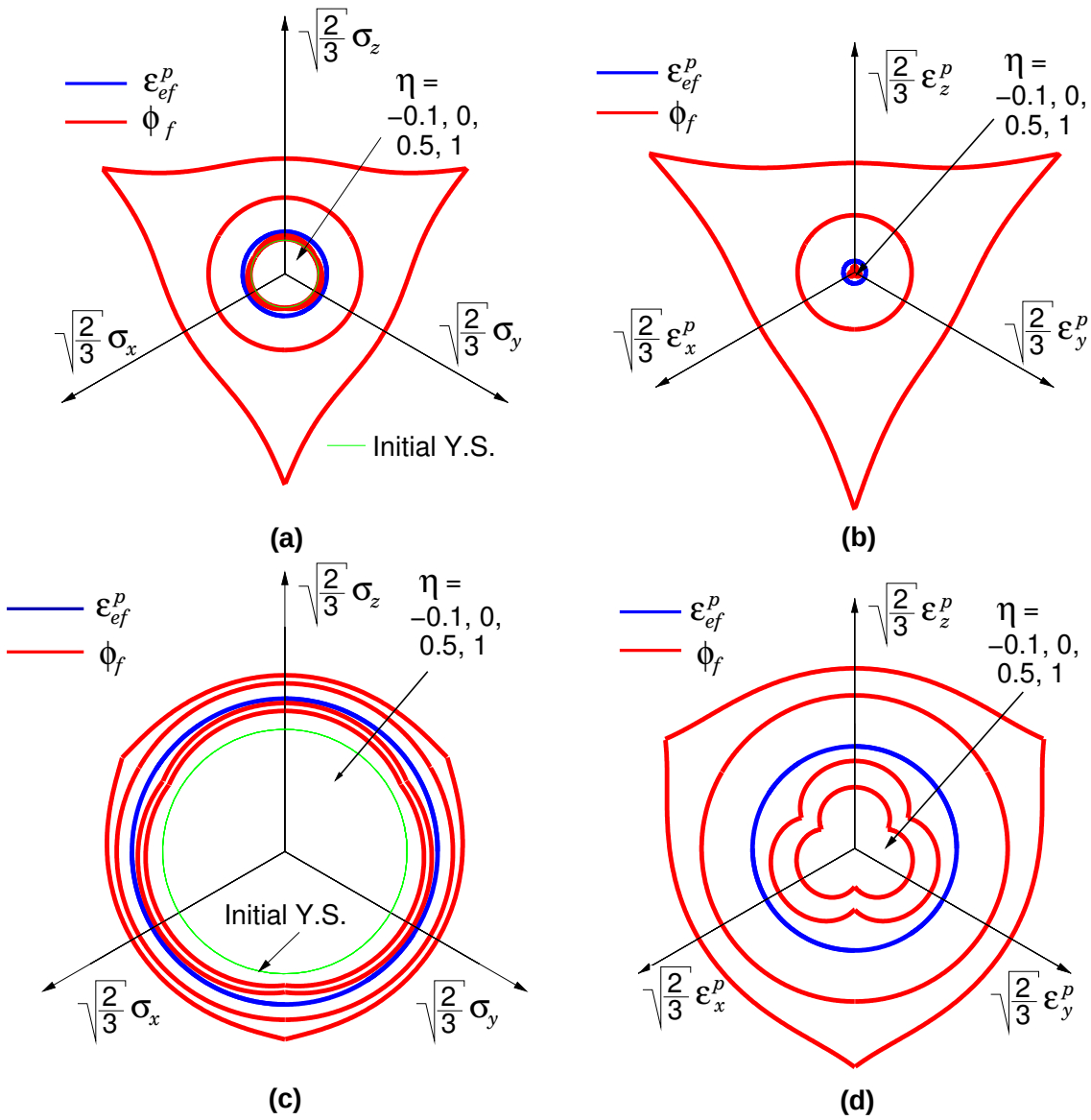

Figure 20: Stress and plastic strain states at failure according to the tearing parameter failure criterion for 3D, proportional stress paths. (a) Stress space, $\xi = 4$, (b) plastic strain space, $\xi = 4$, (c) stress space, $\xi = 1$ and (d) plastic strain space, $\xi = 1$.

the value of ξ can be picked by the analyst, it is expected that calibrating both ξ and ψ_f to experimental data can lead to improved failure predictions.

Proportional Stress Paths–Three-Dimensional Results

In order to determine the failure envelope according to this criterion, the largest principal stress has to be determined first. As was done in the case of the maximum shear stress criterion, the range $-1/2 \leq \alpha \leq 1$ with $s > 0$ is considered. In this range $\sigma_1 = \sigma_x = \sigma_m + s$.

Substituting into (47) gives

$$\psi = \int_0^{\varepsilon_e^p} \left\langle \frac{2\left(\sigma_m + s\right)}{3s} \right\rangle^{\xi} \mathrm{d}\hat{\varepsilon}_e^p. \tag{49}$$

Dividing the numerator and denominator of the quantity in the brackets by σ_e and using (8), (16) and (22) yields

$$\psi = \int_0^{s} \left(\frac{2}{3}\right)^{\xi} \left\langle \eta\sqrt{3(1+\alpha+\alpha^2)} + 1 \right\rangle^{\xi} \frac{\sqrt{3(1+\alpha+\alpha^2)}}{E_t^p} \mathrm{d}\hat{s}. \tag{50}$$

Since η, α and E_t^p are all constants, this expression can be easily integrated to give

$$\psi = \left(\frac{2}{3}\right)^{\xi} \left\langle \eta\sqrt{3(1+\alpha+\alpha^2)} + 1 \right\rangle^{\xi} \frac{\sqrt{3(1+\alpha+\alpha^2)}}{E_t^p} \left(s - \bar{s}_o\right). \tag{51}$$

where $\bar{s}_o$ is the value of s at yield as given by (17). Note that in order for ψ to be non-zero,

$$\eta\sqrt{3(1+\alpha+\alpha^2)} + 1 > 0. \tag{52}$$

This expression sets some limits for η for given values of α. Values of η more negative than these limits completely prevent failure from occurring. For example, for $\alpha = -\frac{1}{2}, 0, 1$, $\eta > -\frac{2}{3}, -\frac{1}{\sqrt{3}}, -\frac{1}{3}$ respectively.

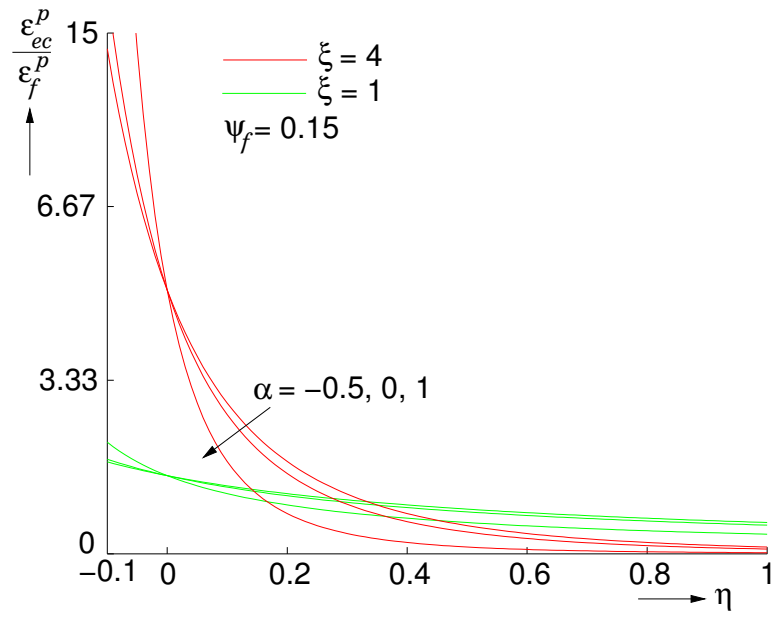

Figure 21: Predicted variation by the tearing parameter for the critical value of the equivalent plastic strain with triaxiality for three values of α and two values of ξ.

If (52) is satisfied, then at failure $\psi = \psi_f$, and (51) can be solved for the critical value value of s, which gives

$$s_c = \left(\frac{3}{2}\right)^{\xi} \frac{\psi_f}{\left(\eta\sqrt{3(1+\alpha+\alpha^2)} + 1\right)^{\xi}} \frac{E_t^p}{\sqrt{3(1+\alpha+\alpha^2)}} + \bar{s}_o \tag{53}$$

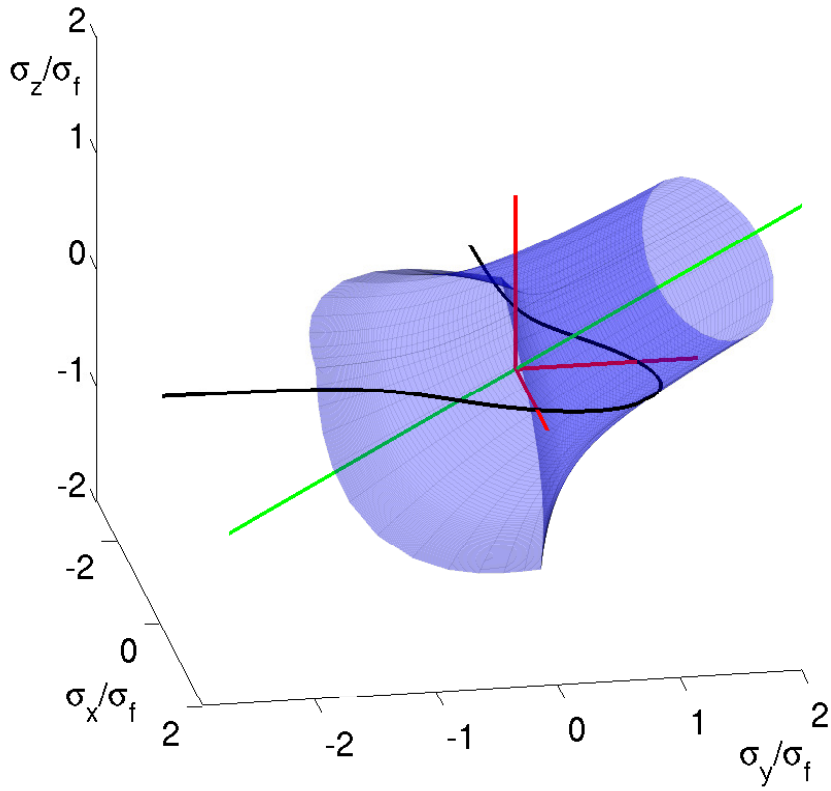

Figure 22: The tearing parameter failure surface in principal stress space for 3D proportional stress paths ($\xi = 1$). The hydrostatic axis is shown in green and the origin is shown by the intersection of the three red axes. The black line is the intersection with the σ_x-σ_y plane.

and the stress components can then be determined from (14) and (15). Clearly the shape of the failure surface is complex. When $\eta = 0$, however, it can be shown that

$$\varepsilon^p_{ec} = \left(\frac{3}{2}\right)^{\xi} \psi_f.$$

In other words, the shape of the failure surface contour when $\eta = 0$ is a circle. Its radius depends on the values of the tearing parameter at failure ψ_f and the exponent ξ. At the other extreme, as η goes to infinity (hydrostatic tension), (53) reduces to $s_c = \bar{s}_o$. This means that the tearing parameter predicts nearly immediate failure for high triaxiality stress paths.

The contours of the failure surface obtained for constant triaxiality in principal stress and strain space are shown in Fig. 20. Contours based on the recommendation presented by Wellman and Salzbrenner (1992) that $\xi = 4$, are plotted in Fig. 20(a) and (b). The contours obtained with the equivalent plastic strain criterion are shown in blue for comparison purposes. Clearly, the failure criterion has a strong dependence on triaxiality. Note that the contours become quite large compared to those generated by the equivalent plastic strain criterion when the triaxiality is zero or negative. This is most apparent when looking at the

strain contours in Fig. 20(b). The effect of triaxiality can be moderated by choosing smaller values of ξ, as shown in Fig. 20(c) and (d), which were generated with $\xi = 1$. Clearly the criterion shows Lode angle dependence if $\eta \neq 0$ as evidenced by the non-circular shapes of the contours.

To further demonstrate the effect of ξ, Fig. 21 shows the triaxiality dependence of the equivalent plastic strain at failure for three values of α. Due to the Lode angle dependence, the three values of α produce distinct curves. Note that increasing ξ makes the failure criterion more sensitive to the effects of triaxiality. This implies a reduction of the strain to failure for triaxialities higher than $\eta = 1/3$, and greatly increasing the strain to failure for triaxialities lower than 1/3.

The three-dimensional failure surface obtained with $\xi = 1$ is shown in Fig. 22, with the projection onto plane stress shown in black line. Clearly, under plane stress, failure is inhibited when both stress components are compressive. To maintain clarity in the figure the surface is plotted for values of η that satisfy (52) by some margin.

Proportional Stress Paths–Plane Stress Results

Applying the tearing parameter failure criterion to proportional loading under plane stress gives the red envelopes shown in Fig. 23. The failure envelope in stress space is shown in Fig. 23(a) compared to the blue ellipse obtained with the equivalent plastic strain criterion. Three curves are shown for the tearing parameter, corresponding to values of $\xi = 4$, 1 and 0.25. Note that as ξ increases, failure occurs at lower stress combinations in the vicinity of the equi-biaxial stress path, and at higher stresses in the vicinity of pure shear. The failure envelopes in plastic strain space, shown in Fig. 23(b), also reflect these observations. Note that for equi-biaxial stressing and $\xi = 4$ failure actually occurs soon after initial yield as seen in Fig. 23(a), and therefore the plastic strains at failure are also very small. At the same time, the strains at failure for the pure shear case are very large. Reducing the value of ξ makes the failure envelopes approach that of the equivalent plastic strain criterion, as long as one of the two stresses is positive.

Figure 23(c) reflect the observations made previously. Note that increasing ξ causes a reduction on the critical equivalent plastic strain to failure for $\eta > 1/3$ but a marked increase when $\eta < 1/3$.

4.6 Johnson-Cook

Definition

Johnson and Cook (1985) proposed plasticity and failure models that account for factors that are important when materials are loaded to failure at high rates. These factors include large strains, large strain rates, high pressures and high temperatures.

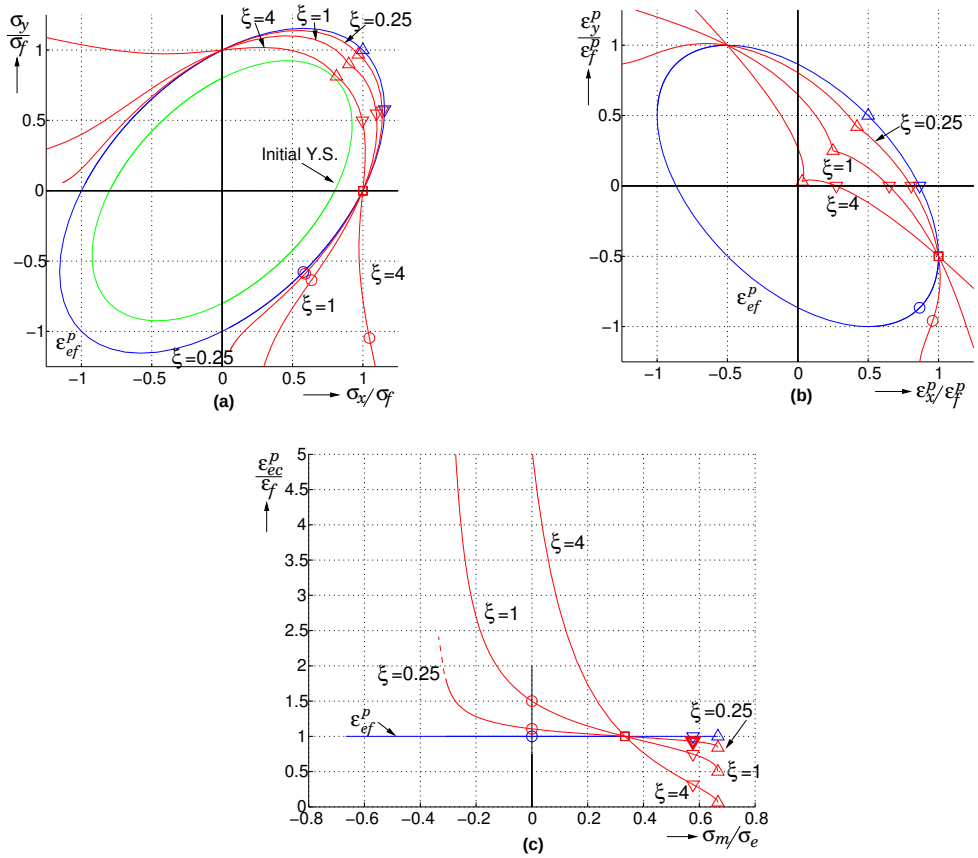

Figure 23: Tearing parameter failure criterion for plane stress, proportional stress paths. (a) Stress space, (b) in-plane plastic strain space, (c) critical equivalent plastic strain vs. stress triaxiality. The results from the equivalent plastic strain criterion are shown for reference in blue line.

The model to calculate plastic deformation (often called the "strength model") assumes that plastic deformation is governed by the J_2 flow theory of plasticity, but that the expression for the equivalent stress-plastic strain (σ_e-ε_e^p) curve of the material during plastic loading depends not only on equivalent plastic strain, but also on strain rate and temperature. The influences of each of these parameters are decomposed in a multiplicative manner as follows:

$$\sigma_e = \left[A + B\left(\varepsilon_e^p\right)^n\right]\left[1 + C\ln\left(\frac{\dot{\varepsilon}_e^p}{\dot{\varepsilon}_{eo}^p}\right)\right]\left[1 - \hat{T}^m\right] \tag{54}$$

Here, $(\dot{\bullet}) = d(\bullet)/dt$ where t represents time, $\dot{\varepsilon}_{eo}^p$ represents a reference strain rate and

$$\hat{T} = \begin{cases} 0, \text{ if } T < T_r \\ \frac{T-T_r}{T_m-T_r}, \text{ if } T_r \leq T \leq T_m \\ 1, \text{ if } T > T_m \end{cases} \tag{55}$$

is the homologous temperature. In the latter expression, T, T_r and T_m are the current temperature, a reference (usually room) temperature and the melting temperature of the

material[3] Finally, the five parameters (A, B, n, C, m) are adjusted to match as well as possible the data obtained from material tests. Note that testing data obtained under quasi-static and dynamic conditions as well as at temperature are needed to fit this model.

Since the objective of the present work is to review failure criteria, the strength model will not be exercised here. Instead, the simple rate and temperature independent model used in all the previous examples will still be used.

The failure model is also constructed using a multiplicative decomposition of the effect of triaxiality, strain rate and temperature on the equivalent plastic strain at failure:

$$\varepsilon^p_{ef} = \left[d_1 + d_2 e^{d_3 \eta}\right] \left[1 + d_4 \left(\frac{\dot{\varepsilon}^p_e}{\dot{\varepsilon}^p_{eo}}\right)\right] \left[1 + d_5 \hat{T}\right] \tag{56}$$

where $d_1, \ldots, d_5$ are adjusted to best represent the dependence of the equivalent plastic strain at failure. Note that the dependence of the equivalent plastic strain at failure on triaxiality has an exponential form, as suggested by Rice and Tracey (1969) for the enlargement of spherical voids. Since the values of η, $\dot{\varepsilon}^p_e$ and $\hat{T}$ can vary during the loading history at a material point, a cumulative damage variable is defined as

$$D = \int_0^{\varepsilon^p_e} \frac{\mathrm{d}\hat{\varepsilon}^p_e}{\varepsilon^p_{ef}(\eta, \dot{\varepsilon}^p_e/\dot{\varepsilon}^p_{eo}, \hat{T})} \tag{57}$$

with failure occurring when $D = 1$.

Examples of Use

Because of its simplicity and dependence on triaxiality, strain rate and temperature, the Johnson-Cook model is widely used to predict material plastic flow and failure. Whereas the strength model has been called a "workhorse for engineers and analysts," (Dabboussi

[3]Temperature changes in the material may be due to environmental conditions or to heat generated from plastic deformation. The heat generated during plastic deformation is often calculated as

$$dq = \beta\, \sigma\, d\varepsilon^p_e,$$

where the parameter β represents the fraction of plastic work that is converted into heat. Generally β is taken to be a constant in the order of 0.90 to 0.95, but experiments show that it can depend on strain and strain rate as discussed by Mason *et al* (1994). It appears, however, that assuming constant values in the order of 0.90 to 0.95 is a good approximation, especially as the strains become larger, at least for the Al 2024 and 4340 steel specimens that they tested. The importance of plastic dissipation depends on the temperature sensitivity of the material and the rate that heat is transported away from local hot zones. For sufficiently slow rates, the heat generated by plastic work dissipates without a significant temperature increase in the material ($\Delta T \approx 0$). For sufficiently fast strain rates, ΔT can be calculated by assuming adiabatic heating as follows:

$$\Delta T = \frac{\beta}{\rho\, C_p} \int \sigma\, \mathrm{d}\varepsilon^p_e$$

where ρ is the density of the material, and C_p is the specific heat capacity. For intermediate strain rates, one must solve the coupled thermo-mechanical boundary value problem to calculate the temperature rise ΔT.

and Nemes (2005)), examples where the failure criterion has been calibrated seem to be significantly more sparse. Johnson and Cook (1985) indicate that, for the materials they considered, failure seems to be more dependent on triaxiality and less so on strain rate and temperature. A similar conclusion has also been reached by Skoglund *et al* (2006) after fitting the failure criterion for a high performance armor steel.

The use of the Johnson-Cook strength and failure models seem to be particularly prevalent in the field of ballistic impact simulation. For example Borvik *et al* (2005) as well as Teng and Wierzbicki (2006) used these models to numerically simulate the impact of high speed projectiles on Al 6005-T6 panels and Weldox 460 steel plates and compared the results to experimental data. Both reported that using the Johnson-Cook model gave very good predictions of different aspects of the impact events such as the prediction of the ballistic limit, the residual velocity after perforation and the crack patterns. Similar conclusions have also been reached by Corona *et al* (2013) for simulations of impact and puncture of Al 7075-T651 plates by a punch attached to a large mass.

One of the keys to success in the references given above was that in all cases relatively comprehensive experimental studies of the material response and failure were conducted to provide data for the calibration of the strength and failure models. The material tests required for the full calibration of the models are, at a minimum: Quasi-static uniaxial tension tests at room temperature, quasi-static uniaxial tension tests at different temperatures, quasi-static tension tests on notched specimens, and high strain rate uniaxial tension tests. If the problem being solved is insensitive to some of the parameters of the model, however, the material tests listed above that are not relevant do not have to be conducted.

Proportional Stress Paths–Three Dimensional Results

Although the model allows for the equivalent plastic strain at failure to depend on strain rate and temperature, the only effect that will be considered in this review is that of triaxialtiy. Under these conditions (56) reduces to

$$\varepsilon^p_{ef} = d_1 + d_2 e^{d_3 \eta}, \tag{58}$$

and (57) to

$$D = \int_0^{\varepsilon^p_e} \frac{\mathrm{d}\hat{\varepsilon}^p_e}{\varepsilon^p_{ef}(\eta)}. \tag{59}$$

Since η is fixed for the proportional paths considered in Section 3.1, the critical value of equivalent strain at failure, ε^p_{ec}, will be equal to the value given by (58), in other words

$$\varepsilon^p_{ec} = \varepsilon^p_{ef}.$$

From (23) and (17) one obtains the expression for the critical value of s as

$$s_c = \frac{E^p_t \varepsilon^p_{ef} + \sigma_o}{\sqrt{3(1+\alpha+\alpha^2)}}. \tag{60}$$

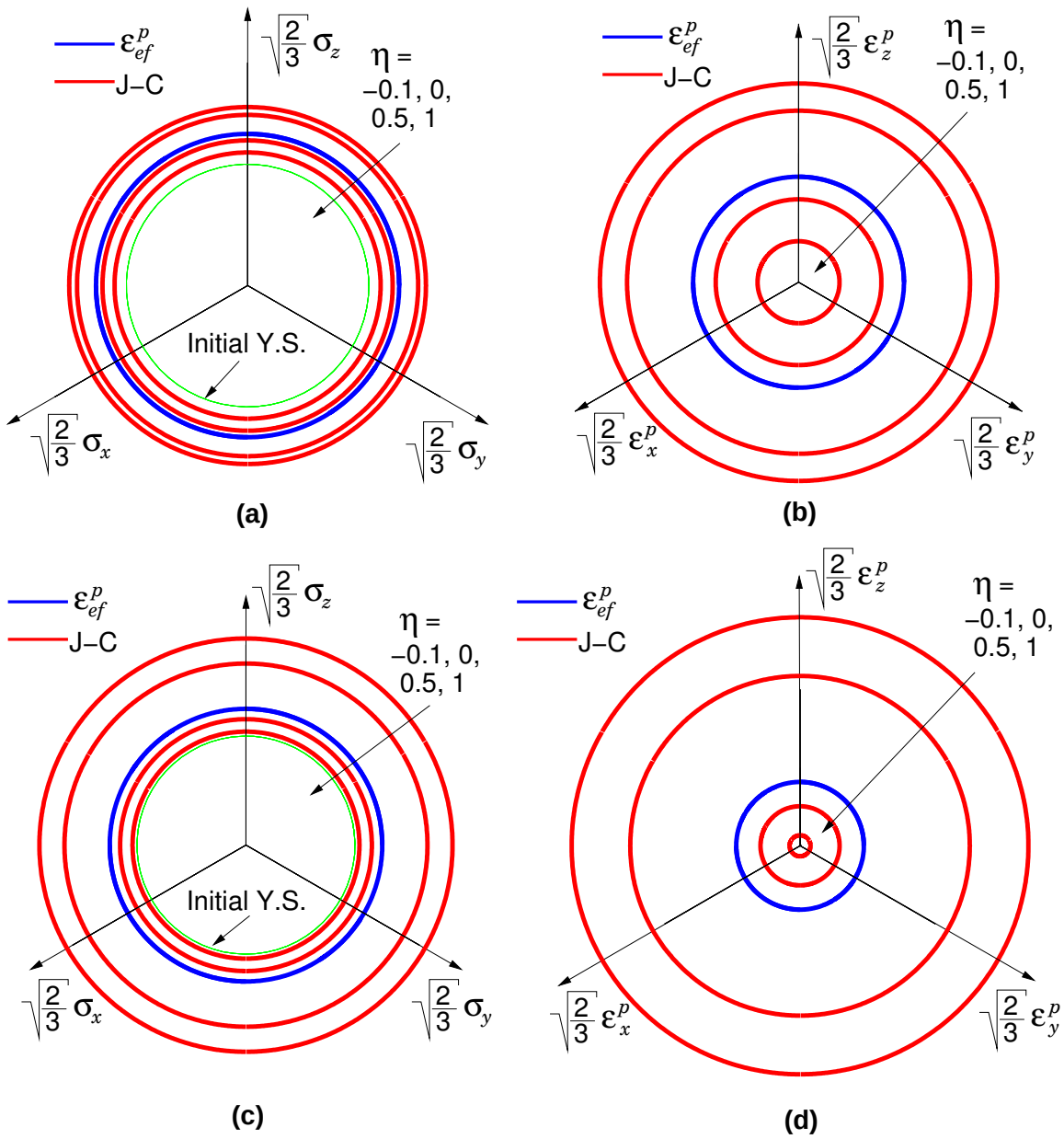

Figure 24: Stress and plastic strain states at failure according to the Johnson-Cook failure criterion for 3D proportional stress paths. (a) Stress space, case 1, (b) plastic strain space, case 1, (c) stress space, case 2 and (d) plastic strain space, case 2. Case 1: $d_1 = 0.005, d_2 = 0.34, d_3 = -1.5$. Case 2: $d_1 = 0.005, d_2 = 0.39415, d_3 = -3$.

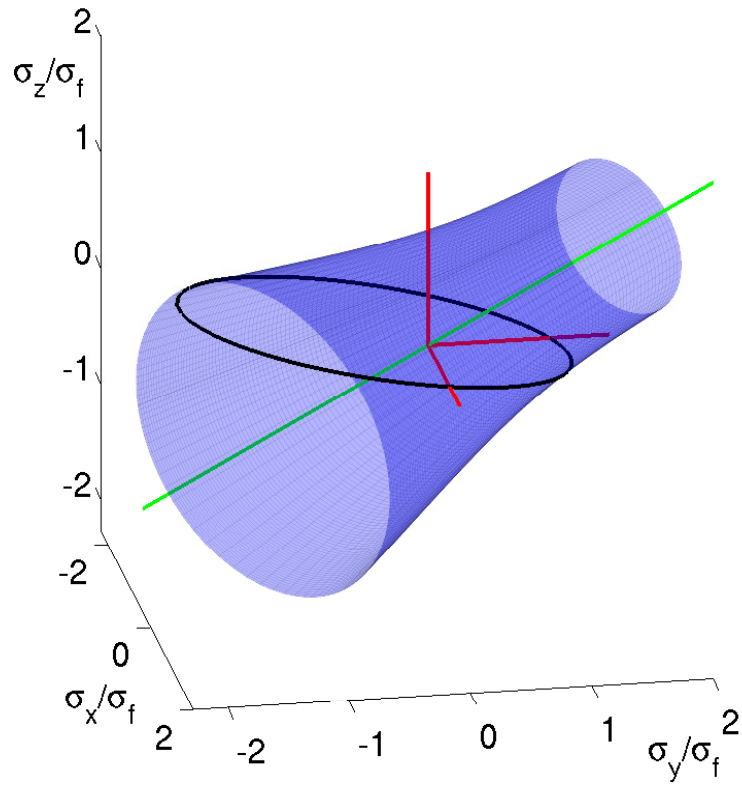

Figure 25: The Johnson-Cook failure surface in principal stress space for 3D proportional stress paths ($d_1 = 0.005, d_2 = 0.34, d_3 = -1.5$). The hydrostatic axis is shown in green and the origin is shown by the intersection of the three red axes. The black line is the intersection with the σ_x-σ_y plane.

Also note that substituting (16) into (60) gives the critical value of the equivalent stress at failure as

$$\sigma_{ec} = E_t^p \varepsilon_{ef}^p + \sigma_o. \tag{61}$$

This latter equation, in conjunction with (58), indicates that σ_{ec} depends on η only, so this failure criterion does not have Load angle dependence.

Figure 24 shows examples of stress and plastic strain contours at failure predicted by this failure criterion for four values of triaxiality. In all cases, the parameters d_1, d_2 and d_3 were adjusted to result in failure under uniaxial conditions at a strain of 0.15. The contours produced by the equivalent plastic strain criterion are shown in blue line, while the initial yield surface is shown in green line for reference. Figures 24(a) and (b) show contours for the case with $d_1 = 0.005$, $d_2 = 0.239$ and $d_3 = -1.5$. These values give a relatively moderate dependence of failure on triaxiality as compared to the cases in Fig. 24(c) and (d), which were generated with $d_1 = 0.005$, $d_2 = 0.39415$ and $d_3 = -3$. Note that all contours are circular indicating no dependence on Lode angle as mentioned previously.

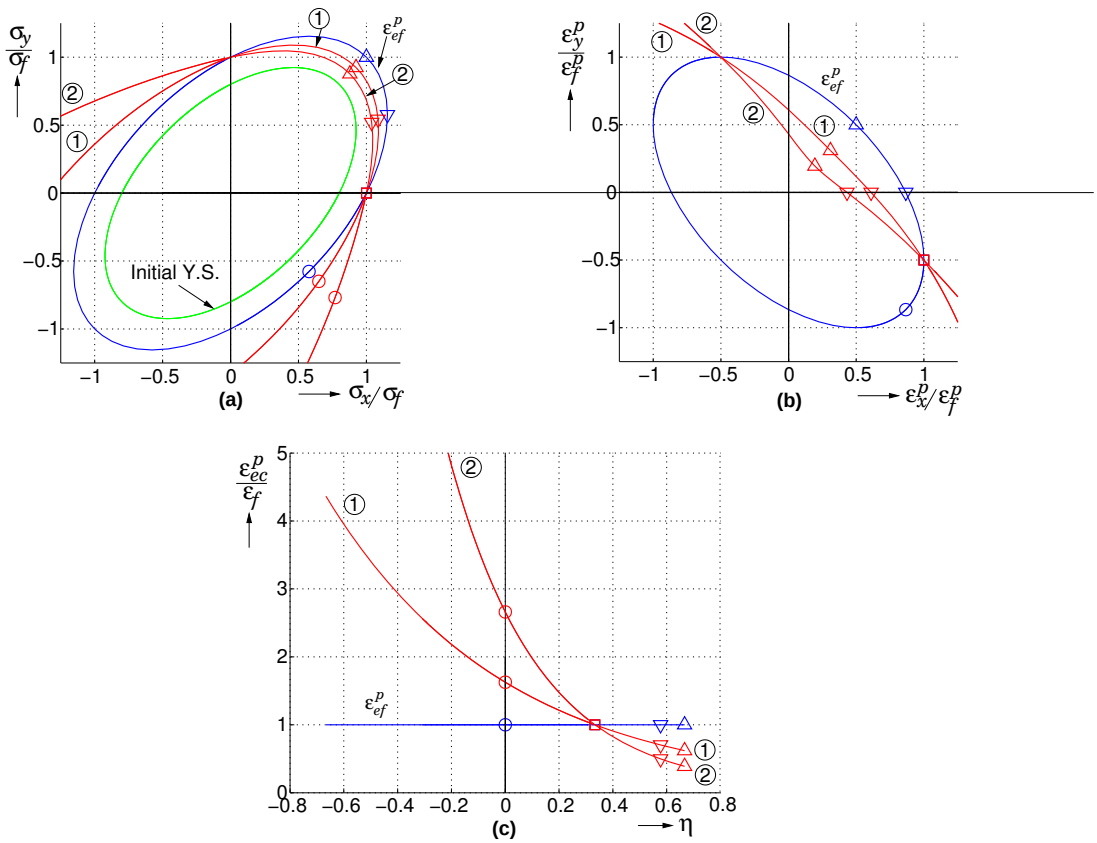

Figure 26: The Johnson-Cook failure criterion for plane stress, proportional stress paths. The two cases shown correspond to those shown in Fig. 24. (a) Stress space, (b) in-plane plastic strain space, (c) critical equivalent plastic strain vs. stress triaxiality. The results from the equivalent plastic strain criterion are shown for reference in blue line.

The failure surface generated with $d_1 = 0.005$, $d_2 = 0.239$ and $d_3 = -1.5$ is shown in Fig. 25 together with the hydrostatic axis in green line and the projection onto the σ_x-σ_y plane in black line. Note that the Johnson-Cook failure criterion produces a closed line in plane stress as shown. This is in contrast with the equivalent plastic strain in tension and the tearing parameter criteria, which produce open failure envelopes in plane stress, resulting in infinite strength under stress states dominated by biaxial compression. The strength of the material predicted by the Johnson-Cook model, however, is still much larger when the stresses are compressive than when they are tensile. In this respect, it resembles the Mohr-Coulomb criterion.

Proportional Stress Paths–Plane Stress Results

Applying the Johnson-Cook failure criterion to proportional loading under plane stress gives the results in Fig. 26. Failure curves in stress space are shown in Fig. 26(a) for the two cases presented earlier in Fig. 24. The stress range shown cuts the contours off, but recall that

they are actually closed for much larger compressive stresses than shown. The corresponding failure curves in strain space are given in Fig. 26(b). Finally, the dependence of the equivalent plastic strain on triaxiality is shown in Fig. 26(c). Note that these curves represent the definition of the failure criterion as stated in (58).

4.7 BCJ_MEM

Definition

BCJ_MEM (Bammann-Chiesa-Johnson Microstructural Evolution Model) is a strain rate and temperature dependent elasto-viscoplasticity model with isotropic damage. Unlike the other models discussed herein, BCJ_MEM's plasticity model is coupled to the damage model. In the limit as the strain rate goes to zero, BCJ_MEM reduces to a classical plasticity model with isotropic damage when the temperature is held well below the melting point. In a dynamic setting, rate and temperature dependencies are activated, which can impact the the strain to failure.

The failure model in BCJ_MEM is history dependent, so it is important to understand how strain rate and temperature affect the plastic response. For the simplified case of uniaxial tension, at a constant strain rate, without kinematic hardening, stage IV hardening, or static recovery, the yield stress curve can be expressed as

$$\sigma_y = (1 - v) \left[\sigma_o + \frac{E_t^p}{R_d} \left(1 - \exp(-R_d \, \varepsilon_e^p)\right) \right] \left\{ 1 + \sinh^{-1} \left[\left(\frac{\dot{\varepsilon}_e^p}{w} \right)^{1/r} \right] \right\}. \tag{62}$$

This equation can be compared with (54) for the Johnson-Cook model. The first expression in parentheses causes the equivalent stress to linearly decay with the percent damage v. The second expression in square brackets includes the initial yield strength σ_o, the linear hardening modulus E_t^p, and the dynamic recovery parameter R_d, which collectively control the rate independent behavior of the model. The third expression in curly brackets contains the equivalent plastic strain rate $\dot{\varepsilon}_e^p$ and two model parameters w and r, which control the rate dependent behavior of the model. Each of these parameters (σ_o, E_t^p, R_d, w, and r) can be material constants, or they can independently vary with temperature T in a variety of ways (see Sierra Solid Mechanics Team (2013) for further details). One should also keep in mind that plastic work in BCJ_MEM gets converted into heat, which can cause a significant temperature rise under the right conditions (see footnote in Section 4.6). Thus, plastic dissipation plays a role in the rate dependence of the model.

The isotropic damage component of BCJ_MEM is based on a void growth model originally proposed by Cocks and Ashby (1980) (Eqns. (32-34)). The growth model does not include void nucleation, so the analyst must provide an initial volume fraction of voids v_o, which can then grow during the simulation. (A void nucleation model, which will augment the void growth model, is under development.) The growth equation for the void volume fraction v

is

$$\frac{\mathrm{d}v}{\mathrm{d}\varepsilon_e^p} = \sqrt{\frac{3}{2}}\,\frac{1-(1-v)^{m+1}}{(1-v)^m}\,\sinh\left[\frac{2\,(2\,m-1)}{2\,m+1}\,\langle\eta\rangle\right], \tag{63}$$

where the damage exponent m is a user specified constant. Failure occurs when

$$v = v_f, \tag{64}$$

where v_f is the void volume fraction at failure, which must be determined by the analyst. The analyst should also pick $m \geq 0.5$ so that the hyperbolic sine term remains positive and voids do not shrink. When voids do grow, they are thought to grow only when $\sigma_m > 0$, so the Macaulay brackets ($\langle\cdot\rangle$) in (63) cause $\mathrm{d}v/\mathrm{d}\varepsilon_e^p = 0$ when $\eta < 0$. Finally, note that (63) does not explicitly include strain rate or temperature, in contrast to the Johnson-Cook failure model.

As opposed to the other failure models considered, damage and plasticity are fully coupled in BCJ_MEM. The accumulation of plastic strain at a given triaxiality affects the void volume fraction (see (63)), and the void volume fraction affects the plasticity by reducing the elastic constants and yield strength. As v increases, Young's modulus and the shear modulus both decrease according to

$$E(T,v) = E(T)\,(1-v), \tag{65}$$

$$\mu(T,v) = \mu(T)\,(1-v), \tag{66}$$

while the yield strength decreases according to (62).

Coupling the plastic response and failure may be more physically realistic than treating them as independent, but it does make the model more difficult to calibrate. For example, plasticity models are typically calibrated against a uniaxial tension stress-strain curve, monotonically loaded to failure. The post-yield engineering stress-strain response can be due to void growth, plasticity, and/or structural effects (necking), so how does one partition these effects? To avoid this dilemma, an analyst needs more experimental data than a monotonically loaded, uniaxial, tension response curve. If one periodically unloads and reloads during the uniaxial tension experiment, it is possible to track the evolution of Young's modulus and indirectly measure v through (65). Alternatively, if one assumes the plasticity is the same in tension and compression, then a uniaxial compression test can be used to calibrate the plasticity parameters in a scenario where voids do not grow.

References and examples of use

The BCJ_MEM development is chronicled in a series of papers starting with Bammann (1990). Since then, several papers have dealt directly with material failure (Bammann *et al*, 1993, 1996; Horstemeyer, 2000) and Hammi *et al* (2004).

Several references exist to help understand the use of BCJ_MEM and its theoretical formulation. The Sierra/SM user manual (Sierra Solid Mechanics Team, 2013) has detailed

descriptions of the material parameters that must be specified to run the model. Brown and Bammann (2012) contains a recent and succinct overview of the model formulation. For a more thorough description of the model, its numerical implementation, and example simulations, see Marin *et al* (2006). (The EMMI model discussed in Marin *et al* (2006) is essentially an alternate formulation of BCJ_MEM without recrystalization.)

Reduction to Linear Hardening

To put BCJ_MEM on equal footing with the other models discussed herein, we must reduce the equivalent stress-equivalent plastic strain relationship (62) to rate-independent, isothermal, linear hardening. First, σ_o, E_t^p, R_d, w, and r become constants. Second, take the limit as w goes to infinity and r goes to zero to remove the rate dependence of the model. Third, employ L'Hôpital's rule to take the limit as R_d goes to zero to obtain

$$\sigma_y = (1 - v)\left[\sigma_o + E_t^p\,\varepsilon_e^p\right]. \tag{67}$$

This expression is close to a linear hardening model, but we must solve for v to complete the simplification.

In the model implementation, v is calculated by numerically integrating (63), but v can be analytically calculated for proportional load paths where η is a constant. Restricting our attention to positive triaxiality ($\langle\eta\rangle = \eta$), we define

$$\gamma(\eta) = \sqrt{\frac{3}{2}}\,\sinh\left[\frac{2\,(2\,m-1)}{2\,m+1}\eta\right], \tag{68}$$

so that (63) can be written as

$$\frac{\mathrm{d}v}{\mathrm{d}\varepsilon_e^p} = \frac{1-(1-v)^{m+1}}{(1-v)^m}\,\gamma(\eta). \tag{69}$$

Next, collect like terms and integrate both sides from the start of plastic deformation to the current state

$$\int_{v_o}^{v} \frac{(1-\hat{v})^m}{1-(1-\hat{v})^{m+1}}\,\mathrm{d}\hat{v} = \int_0^{\varepsilon_e^p} \gamma(\eta)\,\mathrm{d}\hat{\varepsilon}_e^p, \tag{70}$$

to obtain

$$v(\eta, \varepsilon_e^p, v_o, m) = 1 - \left\{1 - \left(1-(1-v_o)^{m+1}\right)\exp\left[(m+1)\,\gamma(\eta)\,\varepsilon_e^p\right]\right\}^{\frac{1}{m+1}}, \tag{71}$$

after some algebraic manipulation.

Note that σ_y becomes non-linear with respect to ε_e^p when we substitute (71) into (67). Linear hardening can still be approximately obtained, however, if v remains small throughout the analysis. To achieve this, we selected an initial void volume fraction of $v_o = 1.0 \times 10^{-4}$ (a

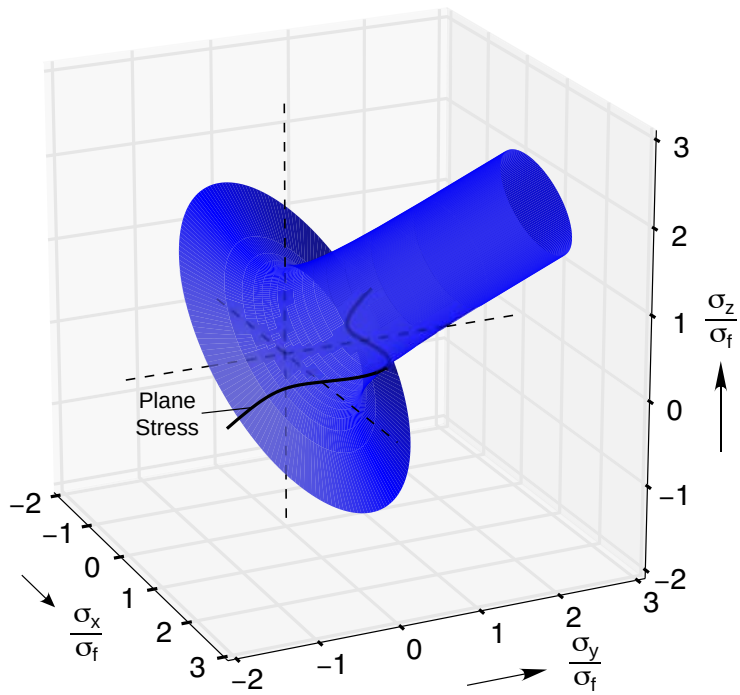

Figure 27: The BCJ_MEM failure surface ($m = 7.0$) in principal stress space for 3D proportional stress paths. The plane stress curve depicts the intersection of the failure surface with the σ_x-σ_y plane.

typical value) and calibrated v_f for several values of m using a uniaxial tension test without any localization ($\eta = 1/3$ and $\varepsilon_f^p = 0.15$). The void fraction at failure is

$$v_f = v\left(\tfrac{1}{3}, 0.15, 1.0 \times 10^{-4}, m\right) \tag{72}$$

$$= 1 - \left\{1 - \left(1 - \left(1 - 1.0 \times 10^{-4}\right)^{m+1}\right) \exp\left[(m+1)\,\gamma\left(\tfrac{1}{3}\right) 0.15\right]\right\}^{\frac{1}{m+1}}. \tag{73}$$

If we set $m = 4.0$ (a typical value), v_f is a small value of 1.5×10^{-4}. If we select a large value of $m = 40.0$, then v_f is still only 8.6×10^{-3}. The function $v\left(\tfrac{1}{3}, 0.15, 1.0 \times 10^{-4}, m\right)$ monotonically increases for the valid range of the damage exponent ($m \geq 0.5$), so any value of m in-between 0.5 and 40.0 will produce virtually linear hardening.

Proportional Stress Paths–Three Dimensional Results

BCJ_MEM's failure model was evaluated using Method A described in Section 3.1. The stress was increased incrementally along each proportional load path using a simple, linear hardening, plasticity model written in Python. The void volume fraction was monitored during each simulation, and the material state was stored at $v = v_f$. The Python code

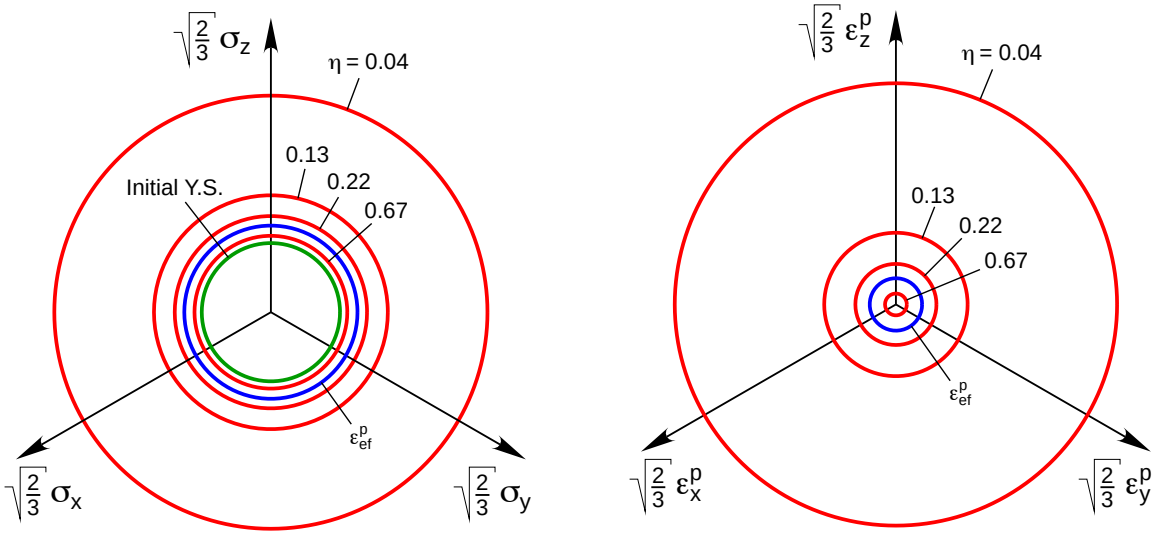

(a) stress contours

(b) plastic strain contours

Figure 28: The BCJ_MEM failure surface ($m = 7.0$) for 3D, proportional, stress paths, projected onto the π-plane. The contours in (a) and (b) show that the failure model does not depend on the Lode angle.

failure predictions were spot checked against the Sierra/SM implementation of BCJ_MEM for three proportional load paths and the results were indistinguishable.

As shown in Fig. 27 for $m = 7.0$, the BCJ_MEM failure surface in 3D principal stress space has a flared end that looks similar to the end of a trumpet. The trumpet shape flares out as the mean stress approaches 0, while the narrow end converges to a cylinder as the mean stress goes to infinity. The intersection between the failure surface and $\sigma_z = 0$ is highlighted with a thick black line to indicate the failure curve for plane stress.

Figure 28a shows the projection of the three-dimensional failure surface (Fig. 27) for $m = 7.0$ onto the π-plane, which looks down the hydrostat. Several stress contours, each at a constant value of η, are compared against the initial yield surface and the equivalent plastic strain criterion. The corresponding plastic strain contours are shown in Fig. 28b. The failure surface is clearly axisymmetric about the hydrostatic axis, meaning the shape can be fully defined in the Rendulic plane.

Looking perpendicular to the hydrostat, the Rendulic plane (Fig. 29) gives a clear view of the failure surfaces for several values of m. Figure 29 plots the Von-Mises equivalent stress at failure σ_{ec} against the mean stress, where we can see that the damage exponent m has a very small impact on the failure surface. The surface only changes slightly when m is increased from 0.5 to 40. (The damage exponent probably has a greater impact when the failure model is calibrated to more ductile materials.) More importantly, the projection onto

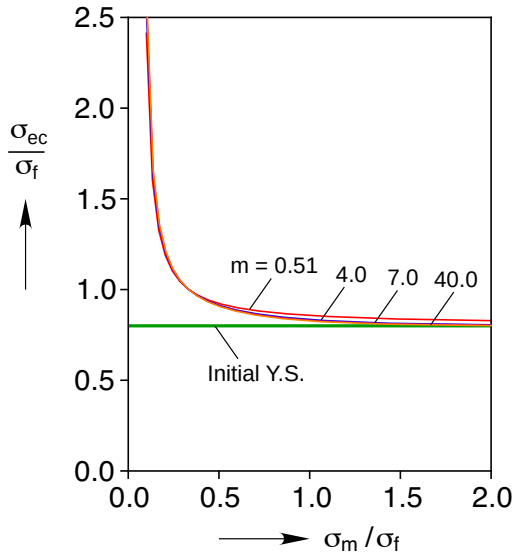

Figure 29: The BCJ_MEM failure surface perpendicular to the hydrostatic axis for several values of m.

the Rendulic plane makes it easy to see that a BCJ_MEM material will never fail in pure shear ($\sigma_m = \eta = 0$). This feature should be expected from (63), since voids require positive triaxiality to grow. (The BCJ_MEM void nucleation model under development is expected to allow voids to nucleate when $\eta \leq 0$.) In addition, the failure surface asymptotes to the yield surface, for all values of m, as σ_m at failure is increased to infinity. This characteristic means that BCJ_MEM predicts failure almost immediately after initial yield for high triaxiality stress paths, similar to the tearing parameter criterion.

Proportional Stress Paths–Plane Stress Results

The plots of stress space, plastic strain space, and triaxiality dependence in Fig. 30 for BCJ_MEM's failure model ($m = 7.0$) all show similar trends under plane stress conditions. First, BCJ_MEM predicts the least ductility for equi-biaxial tension. Second, as we deviate from equi-biaxial tension, the distance between the initial yield surface and the stress space curve increases (Fig. 30a), the plastic strain curve moves further away from the origin (Fig. 30b), and the equivalent plastic strain to failure increases (Fig. 30c). Third, once the stress state reaches pure shear, BCJ_MEM predicts infinite failure stresses and strains.

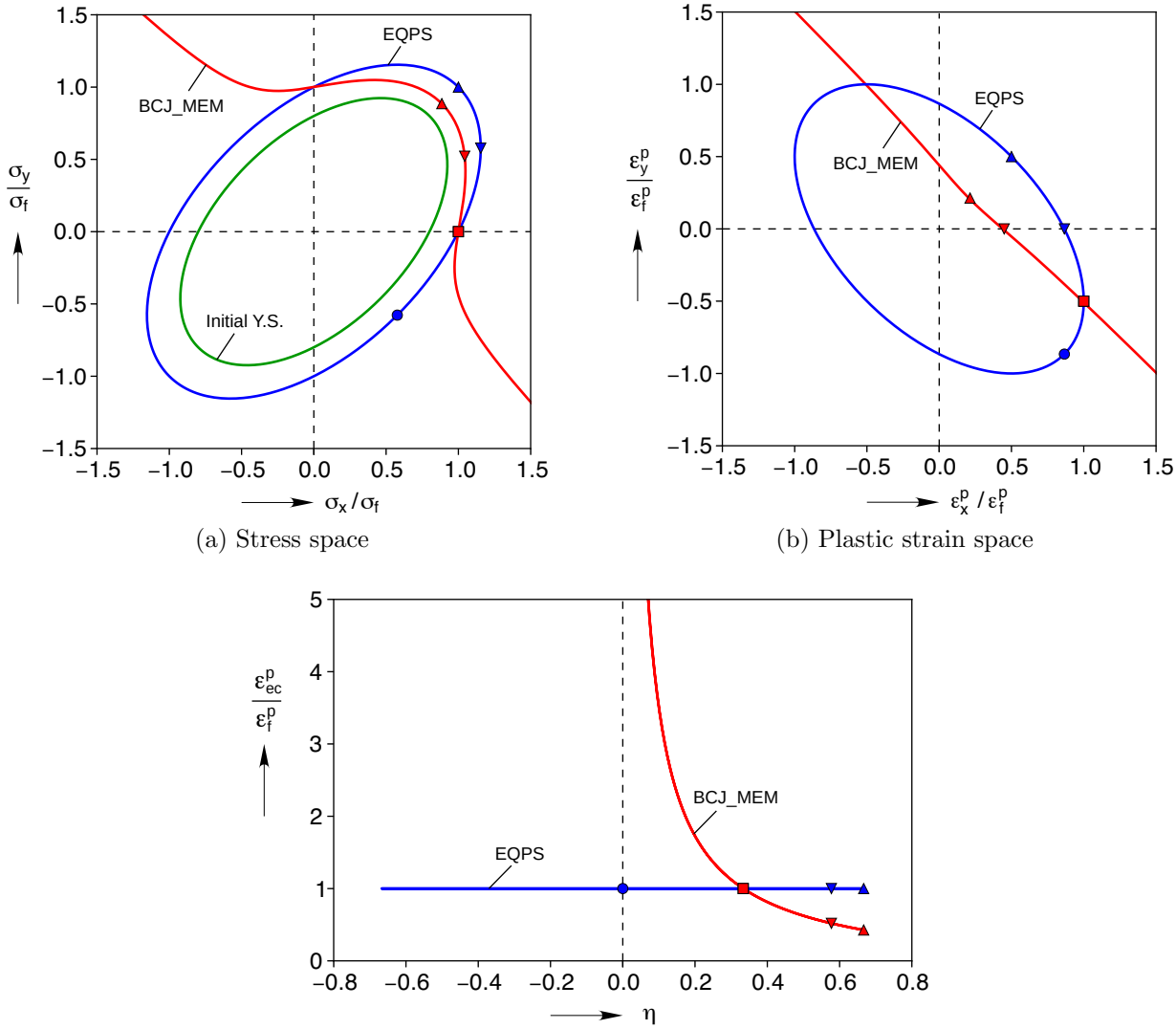

(a) Stress space

(b) Plastic strain space

(c) Triaxiality dependence

Figure 30: The BCJ_MEM failure criterion ($m = 7.0$) for plane stress, proportional stress paths. The results of the equivalent plastic strain criterion are shown for reference in blue line.

5 Summary

This document presented a short survey of ductile failure models to help analysts choose an appropriate failure criteria, and to help interpret the results of analyses. The survey is by no means exhaustive nor detailed. It simply reflects the current understanding of the field by the authors.

The survey concentrated on failure where isothermal and rate-independent conditions prevailed. In many applications, the effects of temperature and strain rate on failure cannot be ignored. These effects, although present in some of the models discussed, were not explored.

Table 3: Summary of ductile failure criteria considered.

Failure Criterion	Triaxiality Dependence	Lode Angle	Failure Model Parameters
Eq. Plastic Stn.	N	N	ε_f^p
Eq. Plastic Stn. in Tens.	Y	N	ε_f^p
Maximum Shear	N	Y	τ_f
Mohr-Coulomb	Y	Y	c_1, c_2
Tearing Parameter	Y	Y	ψ_f, ξ
Johnson-Cook	Y	N	d_1, d_2, d_3
BCJ-MEM	Y	N	v_o, v_f, m

Table 3 presents a summary of the models considered, indicates whether the models exhibit dependence on triaxiality and Lode angle, and lists the parameters that must be calibrated from test data. Dependence on triaxiality seems to be a well accepted feature of ductile fracture, and several of the models include it. The effect of Lode angle dependence of ductile failure models has also been reported, but may be more difficult to calibrate. Mohr-Coulomb and Tearing Parameter exhibit Lode angle dependence and triaxiality dependence, but they are coupled. In other words, one cannot alter the Lode angle dependence without altering the triaxiality dependence. Other models not covered here may not have this constraint.

All the models presented are phenomenological and, as such, should be calibrated with data obtained from material experiments. Furthermore, the best results can be expected if the material calibration experiments are conducted in stress, temperature and loading rate regimes that are close to those that are critical to failure in the applications of interest. In addition, obtaining the best results requires that testing be conducted on samples taken from the same alloy and from parent material that has undergone the same processing as the material in the application of interest. Of course, cutting samples from the same stock as in the application is most preferred. Tests that have been used for calibration include uniaxial tension tests, tension tests on notched specimens, upsetting tests, tension/torsion tests on tubular specimens, Arcan-type tests, etc.

Analysts frequently must decide whether to use a simple or a sophisticated material model. Simple models may be easier to calibrate, but one must keep in mind that such models generally have strong assumptions that may or may not be applicable in a given problem. In general, it is preferable to obtain more material data and fully calibrate a more flexible model than to use a simpler but more rigid model. In the end, however, practical considerations usually limit the amount of data available, and it is up to the analyst's discretion to decide how to best approach problems that involve ductile failure.

Finally, one must keep in mind that ductile failure is a field of current active research and that no recipe exists that can be applied universally to predict it. Instead, the analyst should approach the field with a sense of curiosity that includes considering different models and understanding their advantages and disadvantages with respect to the problem being solved.

References

Alves, S., Schembri, P., Gruda, J., Glascoe, L., Schoonover, J., Phelan, J. and Maienschein, J.L. 2012. Project Newton Final Report. Modeling and Simulation of Narrowbody Aircraft Vulnerability to On-board Explosives. Final Newton Report 2012-1041.

Bai, Y. and Wierzbicki, T. 2008. A New Model of Metal Plasticity and Fracture with Pressure and Lode Dependence, *International Journal of Plasticity*, V. 24, pp. 1071–1096.

Bai, T. and Wierzbicki,T. 2010. Application of Extended Mohr-Coulomb Criterion to Ductile Fracture. *International Journal of Fracture*, V. 161, pp. 1 –10.

Bammann, D.J. 1990. Modeling Temperature and Strain Rate Dependent Large Deformations of Metals. *Applied Mechanics Reviews*, V. 43, pp. S312–S319.

Bammann, D.J., Chiesa, M.L., Horstemeyer, M.F. and Weingarten, L.I. 1993. Failure in Ductile Materials Using Finite Element Methods. In: Proceedings of the Third International Symposium on Structural Crashworthiness, pp. 1–54.

Bammann, D.J., Chiesa, M.L., & Johnson, G.C. 1996. Modeling large deformation and failure in manufacturing processes. In: 19th International Congress of Theoretical and Applied Mechanics, pp. 359–376.

Bao, Y. and Wierzbicki, T. 2004. On Fracture Locus in the Equivalent Strain and Stress Triaxiality Space, *International Journal of Mechanical Sciences*, V. 46, pp. 81-98.

Barsoum, I. and Faleskog, J. 2007. Rupture Mechanisms in Combined Tension and Shear—Experiments, *International Journal of Solids and Structures* V. 44, pp. 1768-1786.

Beese, A.M., Luo, M., Li, Y., Bai, Y. and Wierzbicki, T. 2010. Partially Coupled Anisotropic Fracture Model for Aluminum Sheets, *Engineering Fracture Mechanics*, V. 77, pp. 1128–1152.

Børvik, T., Clausen, A.H., Eriksson, M., Berstad, T., Hopperstad, O.S. and Langseth, M. 2005. Experimental and Numerical Study of the Perforation of AA6005-T6 Panels, *International Journal of Impact Engineering*, V. 32, pp. 35–64.

Bridgman, P.W. Effects of High Hydrostatic Pressure on the Plastic Properties of Metals *Reviews of Modern Physics* V. 17, pp. 3–14.

Brown, A.A. and Bammann, D.J. 2012. Validation of a Model for Static and Dynamic Recrystallization in Metals. *International Journal of Plasticity*, V. 32, pp. 17–35.

Brozzo, P., Deluca, B., and Rendina, R. 1972. A New Method for the Prediction of Formability Limits in Metal Sheets. In: Proc. 7th biennal Conf. IDDR.

Cocks, A.C.F. and Ashby, M.F. 1980. Intergranular Fracture During Power-law Creep Under Multiaxial Stresses. *Metal Science*, V. 14, pp. 8–9.

Corona, E., Witkowski, W.R., Breivik, N.L., Hu, K.T., Gorman, J.S., Spletzer, M.A., & Cordova, T.E. 2012. ASC V&V L2 Milestone No. 4485 Puncture Failure Predictions. Tech. Rept. SAND2012-7604. Sandia National Laboratories.

Corona, E. and Orient, G.E. 2013. An Evaluation of the Johnson-Cook Model to Predict Puncture of 7075 Aluminum Plates. Tech. Rept. SAND2013-XXXX. Sandia National Laboratories. In preparation.

Crane. N.K. 2013. Personal communication.

Dabboussi, W. and Nemes, J.A. 2005. Modeling of Ductile Fracture Using the Dynamic Punch Test. *International Journal of Mechanical Sciences*, V. 47, pp. 1282–1299.

Dunand, M. and Mohr, D. 2011. On the Predictive Capabilities of the Shear Modified Gurson and the Modified Mohr-Coulomb Fracture Models over a Wide Range of Stress Triaxialities and Lode Angles. *Journal of the Mechanics and Physics of Solids*, V. 59, pp. 1374–1394.

Ebnoether, F. and Mohr, D. 2013. Predicting Ductile Fracture of Low Carbon Steel Sheets: Stress-Based versus Mixed Stress/strain-Based Mohr-Coulomb Model. *International Journal of Solids and Structures*, V. 50, pp. 1055-1066.

Fung, Y.C. 1965. Foundations of Solid Mechanics, Prentice Hall, Inc.

Garrison, W.M. and Moody, N.R. 1987. Ductile Fracture, *Journal of Physics and Chemistry of Solids*, V. 48, pp. 1035–1074.

Ghahremaninezhad, A. and Ravi-Chandar, K. 2011. Ductile Failure in Polycrystalline OFHC Copper *International Journal of Solids and Structures*, V. 48, pp. 3299-3311.

Ghahremaninezhad, A. and Ravi-Chandar, K. 2012. Ductile Failure Behavior of Polycrystalline Al 6061-T6 *International Journal of Fracture*, V. 174, pp. 177-202.

Ghahremaninezhad, A. and Ravi-Chandar, K. 2013. Ductile Failure Behavior of Polycrystalline Al 6061-T6 Under Shear Dominant Loading *International Journal of Fracture*, V. 180, pp. 23–29.

Gurson, A. 1977 continuum Theory of Ductile Rupture by Void Nucleation and Growth: Part I–Yield Criteria and flow Rules for Porous Ductile Media. *Journal of Engineering Materials Technology*, V. 99, pp. 2-15.

Haltom, S.S., Kyriakides, S. and Ravi-Chandar, K. 2013 Ductile Failure Under Combined Shear and Tension, *International Journal of Solids and Structures*, V. 50, pp. 1507–1522.

Hammi, Y., Bammann, D.J. and Horstemeyer, M.F. 2004. Modeling of Anisotropic Damage for Ductile Materials in Metal Forming Processes. *International Journal of Damage Mechanics*, V. 13, pp. 123–146.

Horstemeyer, M.F. 2000. A Numerical Parametric Investigation of Localization and Forming Limits. *International Journal of Damage Mechanics*, V. 9, pp. 255–285.

Johnson, G.R. and Cook, W.H. 1985. Fracture Characteristics of Three Metals Subjected to Various Strains, Strain Rates, Temperatures and Pressures. *Engineering Fracture Mechanics.* V. 21, pp. 31–48.

Kazemahvazi, S., Radford, D., Deshpande, V.S. and Fleck, N.A. 2007. Dynamic Failure of Clamped Circular Plates Subjected to an Underwater Shock. *Journal of Mechanics of Materials and Structures.* V. 2, pp. 2007–2023.

Li, Y., Luo, M., Gerlach, J. and Wierzbicki, T. 2010. Prediction of Shear-Induced Fracture in Sheet Metal Forming. *Journal of Materials Processing Technology*, V. 210, pp. 1858–1869.

Marin, E.B., Bammann, D.J., Regueiro, R.A. and Johnson, G.C. 2006. On the Formulation, Parameter Identification and Numerical Integration of the EMMI Model: Plasticity and Isotropic Damage. Tech. Rept. SAND2006-0200, Sandia National Laboratories.

Mason, J.J., Rosakis, A.J. and Ravichandran, G. 1994. On the Strain and Strain Rate Dependence of the Fraction of Plastic Work Converted to Heat: an Experimental Study Using High Speed Infrared Detectors and the Kolsky Bar. *Mechanics of Materials*, **17**(2), 135–145.

McClintock, F.A. 1968. A Criterion of Ductile Fracture by the Growth of Holes. *Journal of Applied Mechanics.* V. 35, pp. 363–371.

Mendelson, A. 1983. Plasticity: Theory and Application, Robert E. Krieger Publishing Company, Inc.

Nahshon, K. and Hutchinson, J.W. 2008. Modification of the Gurson Model for Shear Failure. *European Journal of Mechanics A/Solids*, V. 27, pp. 1–17.

Puttick, K.E. 1959. Ductile Fracture in Metals, *Philosophical Magazine*, V. 4, pp. 964–969.

Rice, J.R. and Tracey, D.M. 1969. On the Ductile Enlargement of Voids in Triaxial Stress Fields. *Journal of the Mechanics and Physics of Solids*, V. 17, pp. 201–217.

Sierra Solid Mechanics Team. 2013. Sierra/Solid Mechanics VOTD User's Guide. Draft, March 21, 2013, pp. 227-233.

Skoglund, P., Milsson, M. and Tjerberg, A. 2006. Fracture Modelling of a High Performance Armour Steel. *J. Phys IV France*, V. 134, pp. 197-202.

Stoughton, T.B. and Yoon, J.W. 2012. Path Independent Forming Limits in Strain and Stress Spaces *International Journal of Solids and Structures*, V. 49, pp. 3616–3625.

Teng, X. and Wierzbicki, T. 2006. Evaluation of Six Fracture Models in High Velocity Perforation *Engineering Fracture Mechanics*, V. 73, pp. 1653–1678.

Tvergaard, V. 1981. Influence of Voids on Shear Band Instabilities Under Plane Strain Conditions. *International Journal of Fracture*, V. 17, pp. 389–407.

Vallellano, C., Guzman, C. and Garcia-Lomas, F.J. 2007. Prediction of Ductile Failure in the Stretch-Forming of AA2024 Sheets. *NUMIFORM '07 Materials Processing and Design: Modeling Simulation and Applications* Cesar de Sa and A.D. Santos, Editors.

Wellman, G.W. and Salzbrenner, R. 1992. Quasistatic Modeling and Testing of Exclusion Region Barrier Mock-Ups. Tech. Rept. SAND92-0024. Sandia National Laboratories.

Wellman, G.W. 2012. A Simple Approach to Modeling Ductile Failure. Tech. Rept. SAND2012-1343. Sandia National Laboratories.

Wierzbicki, T., Bao, Y., Lee,Y.-W. and Bai, Y. 2005 Calibration and Evaluation of Seven Fracture Methods *International Journal of Mechanical Sciences*, V. 47, pp. 719–743.

DISTRIBUTION:

1	MS 0828	S. Kempka, 1510
1	MS 0557	D. Croessmann, 1520
1	MS 0812	N. Breivik, 1524
1	MS 0812	E. Corona, 1524
1	MS 0812	J. Cox, 1524
1	MS 0812	K. Dion, 1524
1	MS 0840	J. Emery, 1524
1	MS 0840	E. Fang, 1524
1	MS 0812	J. Gorman, 1524
1	MS 0840	S. Grange, 1524
1	MS 0812	K. Gwinn, 1524
1	MS 0812	T. Hinnerichs, 1524
1	MS 0840	J. Koester, 1524
1	MS 0812	D. Lo, 1524
1	MS 0812	K. Long, 1524
1	MS 0812	B. Reedlunn, 1524
1	MS 0889	D. Reedy, 1524
1	MS 0812	W. Scherzinger, 1524
1	MS 0840	J. Argüello, 1525
1	MS 0847	S. Attaway, 1525
1	MS 0812	M. Bailey, 1525
1	MS 0812	J. Bean, 1525
1	MS 0840	T. Fuller, 1525
1	MS 0812	S. Haniff, 1525
1	MS 0812	J. Holland, 1525
1	MS 0840	P. Newell, 1525
1	MS 0840	J. Pott, 1525
1	MS 0824	J. Rath, 1525
1	MS 0840	J. Smith, 1525
1	MS 0840	L. Tuttle, 1525
1	MS 0557	S. Kramer, 1528
1	MS 0557	B. Song, 1528
1	MS 0557	M. Spletzer, 1528
1	MS 0828	K. Hu, 1544
1	MS 0828	G. Orient, 1544
1	MS 0828	W. Witkowski, 1544
1	MS 1026	J. Gruda, 2141
1	MS 1185	A. Gullerud, 5417

1	MS 0757	T. Brown, 6625
1	MS 0757	K. Metzinger, 6625
1	MS 9042	B. Antoun, 8256
1	MS 9042	J. Foulk, 8256
1	MS 9042	W.-Y. Lu, 8256
1	MS 9957	A. Mota, 8256
1	MS 9042	J. Ostien, 8256
1	MS 9042	T. Vogler, 8256
1	MS 9042	A. Brown, 8256
1	MS 9042	M. Chiesa, 8256
1	MS 9042	J. Dike, 8256
1	MS 0899	Technical Library, 9536 (electronic copy)

Sandia National Laboratories